

Astrocyte-secreted neurocan controls inhibitory synapse formation and function

Highlights

- Astrocytes control cortical GABAergic synapse formation via secreted signals
- Astrocyte-secreted NCAN C-terminal fragment controls inhibitory synaptogenesis
- NCAN C-terminal localizes to synapses
- NCAN C-terminal is necessary and sufficient for SST+ inhibitory synaptogenesis

Authors

Dolores Irala, Shiyi Wang,
Kristina Sakers, ...,
Dhanesh Sivadasan Bindu,
Justin T. Savage, Cagla Eroglu

Correspondence

dolores.irala@duke.edu (D.I.),
cagla.eroglu@duke.edu (C.E.)

In brief

The astrocyte-secreted molecules controlling inhibitory synapse formation remained elusive for over a decade. Irala et al. found that astrocyte-secreted neurocan C-terminal fragment controls SST+ inhibitory synapse formation and function in the developing cerebral cortex. These results revealed that astrocytes control specific GABAergic synapse types through distinct molecular mechanisms.



Article

Astrocyte-secreted neurocan controls inhibitory synapse formation and function

Dolores Irala,^{1,7,*} Shiyi Wang,¹ Kristina Sakers,¹ Leykashree Nagendren,¹ Francesco Paolo Ulloa Severino,^{1,2,3} Dhanesh Sivadasan Bindu,¹ Justin T. Savage,⁴ and Cagla Eroglu^{1,2,4,5,6,*}

¹Department of Cell Biology, Duke University Medical Center, Durham, NC 27710, USA

²Department of Psychology and Neuroscience, Duke University, Durham, NC 27710, USA

³Instituto Cajal, CSIC 28002 Madrid, Spain

⁴Department of Neurobiology, Duke University Medical Center, Durham, NC 27710, USA

⁵Duke Institute for Brain Sciences (DIBS), Durham, NC 27710, USA

⁶Howard Hughes Medical Institute, Duke University, Durham, NC 27710, USA

⁷Lead contact

*Correspondence: dolores.irla@duke.edu (D.I.), cagla.eroglu@duke.edu (C.E.)

<https://doi.org/10.1016/j.neuron.2024.03.007>

SUMMARY

Astrocytes strongly promote the formation and maturation of synapses by secreted proteins. Several astrocyte-secreted synaptogenic proteins controlling excitatory synapse development were identified; however, those that induce inhibitory synaptogenesis remain elusive. Here, we identify neurocan as an astrocyte-secreted inhibitory synaptogenic protein. After secretion from astrocytes, neurocan is cleaved into N- and C-terminal fragments. We found that these fragments have distinct localizations in the extracellular matrix. The neurocan C-terminal fragment localizes to synapses and controls cortical inhibitory synapse formation and function. Neurocan knockout mice lacking the whole protein or only its C-terminal synaptogenic domain have reduced inhibitory synapse numbers and function. Through super-resolution microscopy, *in vivo* proximity labeling by secreted TurboID, and astrocyte-specific rescue approaches, we discovered that the synaptogenic domain of neurocan localizes to somatostatin-positive inhibitory synapses and strongly regulates their formation. Together, our results unveil a mechanism through which astrocytes control circuit-specific inhibitory synapse development in the mammalian brain.

INTRODUCTION

Proper brain development depends on the establishment, maturation, and activity of excitatory and inhibitory synapses.¹ Therefore, understanding the cellular and molecular mechanisms underlying excitatory and inhibitory synaptogenesis and how these processes are orchestrated is crucial.

In the mammalian cerebral cortex, 80% of neurons are glutamatergic (excitatory) pyramidal neurons, and 20% are GABAergic (inhibitory) interneurons.^{2,3} Interneurons are classified based on their morphological, transcriptomic, and electrophysiological properties^{4–6} in three major groups: somatostatin (SST), parvalbumin (PV), and serotonin receptor 3A (Htr3a).

Astrocytes, actively control synapse formation and function.^{7–9} Astrocyte-secreted synaptogenic proteins, such as thrombospondins, Sparc1/hevin, glyicans, and chordin-like1, strongly promote excitatory synapse development.^{10–13} Astrocytes also control inhibitory synapse formation and maturation via secreted proteins.^{14,15} Yet, the identities of these synaptogenic signals and whether astrocytes differentially control the formation of specific inhibitory circuits are unknown.

Previously, embryonic hippocampi were used to generate glia-depleted inhibitory and excitatory neuron cultures.^{14,15} Treatment of these neurons with astrocyte-conditioned media (ACM) induced both excitatory and inhibitory synapse formation.^{14,15} The astrocytic factors inducing excitatory synaptogenesis do not induce inhibitory synapse formation,¹⁵ suggesting that astrocytes must promote inhibitory synaptogenesis through distinct pathways. Because neurons were isolated from embryos, it has been hard to distinguish the effects of astrocytic factors on neuronal maturation from their roles in synapse formation. Thus, the identities of the astrocytic factors controlling inhibitory synapse formation remained unknown for more than a decade.

Here, we developed a glia-free neuronal culture system using immuno-panned post-natal cortical neurons, in which ACM robustly induces excitatory and inhibitory synaptogenesis without affecting neuronal survival. Using this system, we identified that astrocyte-secreted chondroitin sulfate proteoglycan neurocan (NCAN) robustly induces inhibitory synaptogenesis.

NCAN is part of the Lectican family of proteins. Lecticans are one of the main components of perineuronal nets (PNNs), an extracellular matrix (ECM) structure surrounding PV+ neuronal



cell bodies.^{16,17} Genetic variations in NCAN are a risk factor for bipolar disorder (BD), schizophrenia (SCZ), and mania.^{18–21} NCAN has three regions: an N-terminal composed of an Ig-module and two Link domains, a central linker domain that carries the glycosaminoglycan (GAG) chains, and a C-terminal composed of two epidermal growth factor (EGF)-like domains, a lectin-like domain, and a sushi domain (ELS domains).²² NCAN is cleaved during post-natal development into two fragments: NCAN N-terminal and C-terminal.²² NCAN N-terminal is involved in PNN formation and function.^{23,24} NCAN N-terminal inhibits Semaphorin 3F-induced spine remodeling, NCAM/EphA3 mediated axonal repulsion, and β 1-Integrin-mediated adhesion and neurite outgrowth.^{25–27} NCAN C-terminal is abundant in the ECM and contains multiple protein domains associated with cell adhesion; however, the role of this fragment in the CNS is underexplored.

We found that NCAN C-terminal ELS domain controls inhibitory synaptogenesis and function in the developing mouse cortex, whereas NCAN deficit does not affect excitatory synapse density or function. The synaptogenic NCAN-ELS domain is localized to presynaptically released neuropeptide somatostatin-positive (SST+) synapses. *In vitro* NCAN-ELS domain specifically induced SST+ inhibitory synaptogenesis. Mutant mice lacking the NCAN-ELS domain displayed severely reduced SST+ synapse numbers and function. SST+ synapse density was rescued *in vivo* by restoring NCAN-ELS expression, specifically in astrocytes. Our results shed light on the role of astrocytes during inhibitory synapse formation and provide a circuit-specific mechanism through which astrocytes control inhibition.

RESULTS

NCAN induces inhibitory synaptogenesis in glia-free cortical neuron cultures

To identify astrocyte-secreted proteins controlling inhibitory synaptogenesis, we optimized a rodent glia-free cortical neuron culture system containing both excitatory and inhibitory neurons. Neurons were isolated from neonatal rat cortices by L1CAM immunopanning. These neurons were cultured over 2 weeks and developed extensive neurites. We also isolated astrocytes from neonatal rat cortices to prepare ACM.²⁸ We treated the neurons with ACM or recombinant proteins at days *in vitro* (DIV) 8 and 11 and fixed them at DIV13 to determine the synaptogenic effects (Figure 1A).

These neuronal cultures contained less than 2% GFAP-positive astroglia, 78% excitatory neurons marked with vesicular glutamate transporter 1 (VGluT1+), and 20% of inhibitory neurons identified with vesicular GABA transporter (VGAT+) staining (Figures 1B and 1C). Both SST+ (~9%) and PV+ (~11%) interneurons were present in these glia-free neuronal cultures at DIV 13 (Figures S1A and S1B).

To study how inhibitory neurons (identified as VGAT⁺) make synaptic contacts with excitatory neurons (identified as VGAT⁻), we labeled inhibitory synapses with presynaptic markers bassoon (active zone) and VGAT (inhibitory synaptic vesicles and neurites) together with the post-synaptic marker gephyrin, a scaffolding protein of inhibitory post-synapses (Figure 1D). We found that rising concentrations of ACM induce the formation of inhibitory synapses in glia-free neurons without

altering the numbers of individual bassoon and gephyrin puncta *in vitro* (Figures 1E, 1F, S1J, and S1K). The addition of ACM did not alter the percentage of VGAT+ inhibitory neurons in these cultures (Figures S1C and S1D), indicating that this increase in inhibitory synapse numbers is not due to the enhanced survival of GABAergic neurons.

To identify the astrocyte-secreted proteins that promote inhibitory synapse formation, we conducted an *in vitro* candidate-based screening. To choose candidates, we cross-referenced three proteomic studies that identified proteins present in the ACM^{12,29,30} with a cell-type-specific RNA expression database from the mouse cortex.³¹ We selected four candidates: clusterin (Clu), alpha-dystroglycan1 (DAG), neurocan (NCAN), and carboxypeptidase E (CPE), based on two criteria: (1) all three proteomic studies identified these candidates to be present in the ACM *in vitro*; (2) their expression is highly enriched in astrocytes compared with other CNS cell types *in vivo* (Figure S1E). We tested each candidate's inhibitory synaptogenic effect *in vitro*. We also tested the effect of TGF- β 1 on glia-free neuronal cultures. TGF- β 1 was previously proposed as an astrocyte-secreted protein inducing inhibitory synapse formation.³² However, proteomic studies have not detected TGF- β 1 in the ACM, and TGF- β 1 is predominantly expressed by microglia *in vivo* and not astrocytes (Figure S1E).³¹ When added to glia-free post-natal cortical neuron cultures, we found that TGF- β 1 does not induce inhibitory synapse formation (Figure S1F).

For our screen, we used ACM (100 μ g/ml) as our positive control and neuronal growth media as our negative control. When added to neuronal cultures, DAG, CPE, or CLU did not induce inhibitory synaptogenesis (Figures S1G–S1I). However, NCAN robustly induced inhibitory synapse formation (Figures 1G and 1H) without altering the abundance of bassoon or gephyrin puncta number (Figures S1J and S1K) and puncta size (Figures S1L and S1M). These results suggest that NCAN is an ACM protein that induces inhibitory synapse formation *in vitro*.

To test whether NCAN also induces excitatory synaptogenesis *in vitro*, we treated neurons with NCAN and stained them with presynaptic markers bassoon and VGluT1 together with post-synaptic marker Homer1 (Figure S1N). We found that NCAN does not promote excitatory synaptogenesis *in vitro* at any of the doses used (Figures 1I and 1J) and does not alter Homer1 puncta number and size (Figures S1O and S1P). These data reveal that NCAN specifically controls inhibitory but not excitatory synapse formation *in vitro*.

Astrocytes express NCAN, which is cleaved during post-natal development

Genetic variations in NCAN are risk factors for BD disorder and SCZ.^{18,19,33} Therefore, our *in vivo* studies focused on the mouse anterior cingulate cortex (ACC), an area of the brain where aberrant neuronal connectivity has been associated with SCZ and BD pathophysiology.^{34–37}

Ncan expression is restricted to the nervous system and is known to be highest in the developing mouse brain.³⁸ We determined the astrocytic *Ncan* expression during the post-natal cortical development (post-natal day [P] 7 through 30) by performing single-molecule fluorescence *in situ* hybridization (smFISH) in Aldh1L1-eGFP mouse line in which all astrocytes

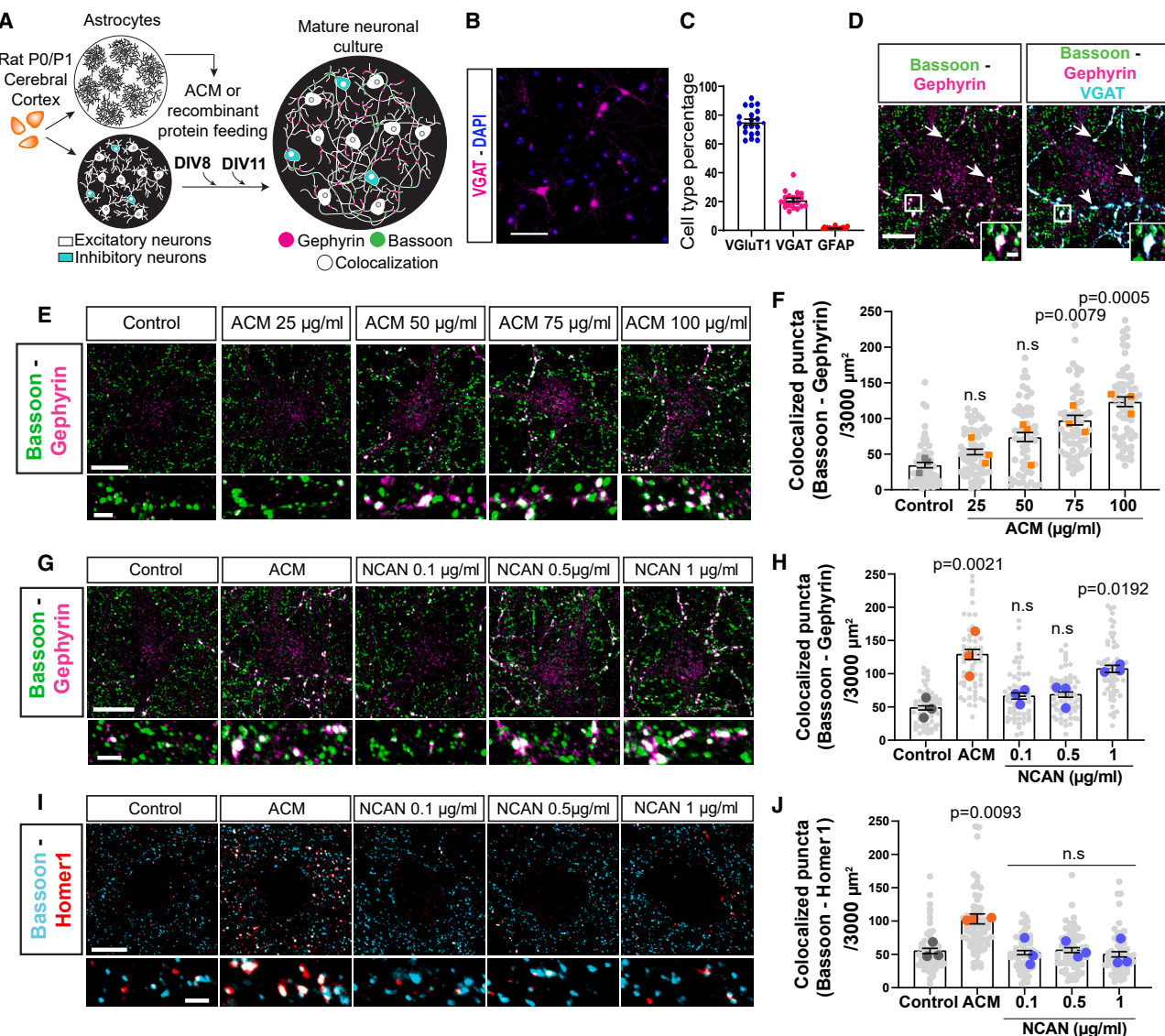
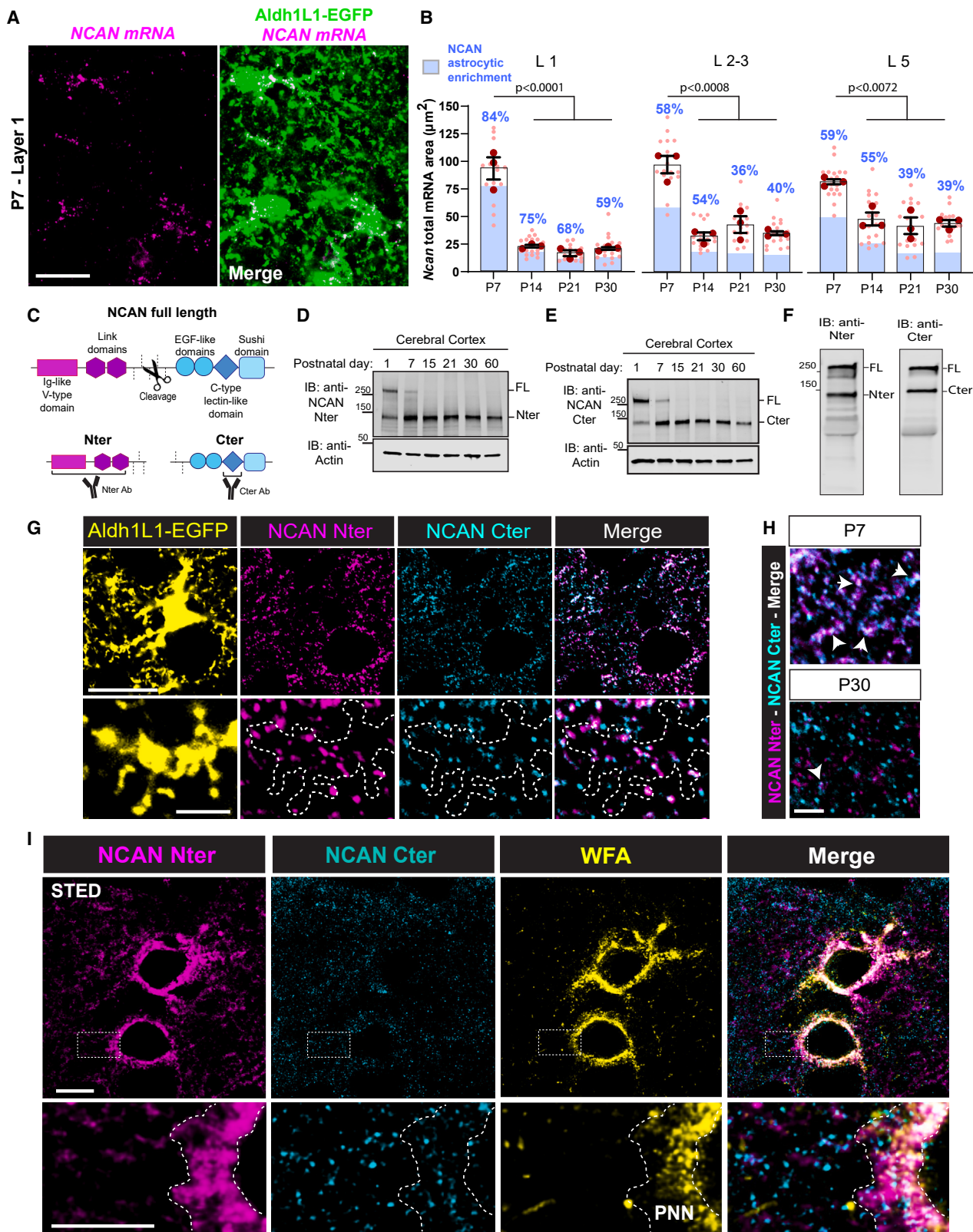


Figure 1. NCAN induces inhibitory synaptogenesis in glia-free neuronal cultures

- (A) Neuronal culture assay and feeding schedule.
- (B) GABAergic interneurons labeled with VGAT. Scale bars, 50 µm.
- (C) Percentage of VGluT1+, VGAT+, and GFAP+ cell types in glia-free neuronal cultures. Data are mean ± S.E.M. 20 images/condition/experiment. n = 3 independent experiments.
- (D) Inhibitory synapses marked with bassoon, VGAT, and gephyrin. Scale bars, 15 µm. Insert scale bars, 2 µm.
- (E) Dose-response curve of ACM. Bassoon and gephyrin mark inhibitory synapses. Scale bars, 20 µm. Insert scale bars, 5 µm.
- (F) Quantification of inhibitory synapses in (E). Data are mean ± S.E.M. n = 3 independent experiments, 20 cells/condition/experiment. One-way ANOVA, Dunnett's post-test.
- (G) Dose-response curve of NCAN recombinant protein. Bassoon and gephyrin mark inhibitory synapses. Scale bars, 25 µm. Insert scale bars, 5 µm.
- (H) Quantification of inhibitory synapses in (G). Data are mean ± S.E.M. n = 3 independent experiments, 20 cells/condition/experiment. One-way ANOVA, Dunnett's post-test.
- (I) Dose-response curve of NCAN recombinant protein. Bassoon and Homer1 mark excitatory synapses. Scale bars, 25 µm. Insert scale bars, 5 µm.
- (J) Quantification of excitatory synapses in (I). Data are mean ± S.E.M. n = 3 independent experiments, 20 cells/condition/experiment. One-way ANOVA, Dunnett's post-test.

express GFP^{39,40} (Figure 2A). We found that from the total of *Ncan*, ~60%–80% or more colocalize with GFP at P7. Interestingly, astrocytes from Layer 1 (L1) have the highest enrichment of *Ncan* compared with astrocytes from Layer 2–3 (L2–3) and

Layer 5 (L5). In all cortical layers, *Ncan* was enriched within GFP+ astrocytes until P21 (Figure S2A). We also found that *Ncan* expression is highest at P7 and its abundance is greatly reduced (~75%) in all the cortical layers by P14 (Figure 2B).



(legend on next page)

These data align with previous RNA sequencing studies showing *Ncan* is enriched in mouse and human astrocytes compared with other brain cell types, and its expression peaks at P7 and gradually reduces at later developmental time points (Figures S2B–S2D). Together, these results indicate that astrocytes are the main source of *Ncan*, which is produced at a high rate during the first post-natal weeks, a period that is followed by accelerated synaptogenesis.

NCAN is known to be cleaved into two halves, generating N- and C-terminal fragments (Figure 2C).^{22,23} To determine the expression and cleavage of NCAN in the developing mouse brain, we used two antibodies specific to N or C-terminals (Figure 2C).

We analyzed NCAN expression in mouse cortical lysates by western blot. Full-length NCAN (250 kDa) was only present in P1 and P7 lysates. By contrast, N- and C-terminal fragments were abundant across development (Figures 2D and 2E). Next, we analyzed the expression of each fragment in the ACM by western blotting. We found that NCAN full-length and N- and C-terminal fragments can be detected in the ACM (Figure 2F). Moreover, we immunostained NCAN in the ACC of *Aldh1L1-eGFP* mice. We found that at P7, NCAN N- and C-terminal are abundant within astrocytes (Figure 2G), and most N- and C-terminal signals overlap. However, by P30, they exhibit distinct localizations in the ECM (Figure 2H). These results show that astrocyte-secreted NCAN is cleaved into two distinct fragments in the brain in a developmentally regulated manner and may conduct distinct functions in the cerebral cortex.

To determine the relative distributions of NCAN N- and C-terminal to the PNNs,^{17,22} we used super-resolution stimulated emission depletion (STED) microscopy in L2-3 of the ACC of P30 wild-type (WT) mice. As previously reported, NCAN N-terminal colocalizes with *Wisteria floribunda agglutinin* (WFA), a PNN marker. However, we found the C-terminal rather distributed in the brain parenchyma (Figure 2I). These results show that astrocytes express NCAN in the developing cortex, and after cleavage, the resulting N- and C-terminal fractions differentially localize in the ECM.

NCAN loss impairs inhibitory synapse formation and function *in vivo*

We generated a transgenic knockout mouse line to study if NCAN is required for inhibitory synaptogenesis *in vivo*. NCAN expression is restricted to the nervous system and is rapidly up-regulated starting at birth.^{31,38,41,42} Moreover, it has a long half-life with an extremely slow protein turnover,⁴³ and astrocytes are the primary cells expressing it. Therefore, a conditional targeting

approach in astrocytes may be ineffective at depleting NCAN during synaptogenesis.

We designed the *Ncan*-null allele (*Ncan* KO) by deleting the exons 3 and 4 via a CRISPR/Cas9-mediated targeting strategy (Figure 3A). We confirmed the successful deletion of *Ncan* via genomic PCR and by immunofluorescence (P10 and P30) and western blotting (P10) (Figures 3B–3D and S3A–S3C).

Loss of NCAN did not affect cortical lamination of the ACC analyzed at P1 by immunofluorescence using the neuronal markers *Lhx2*, *Ctip2*, and *Tbr1* (Figures S3D–S3I). Moreover, we found no difference in the number of GAD67-positive neurons (Figures S3J and S3K) or density of neurons (NeuN+), astrocytes (*Sox9*+/*Olig2*−), or oligodendrocytes (*Olig2*+) between P30 NCAN WT and KO mice in the ACC (Figures S3L and S3M). Finally, we did not observe any differences between NCAN WT and KO mice Mendelian distribution of the litter, litter size, survival rate, body weight, and brain density (Figures S3N–S3R). These results show that loss of NCAN does not cause gross abnormalities, cytoarchitectural deficits, or neuron loss in the ACC.

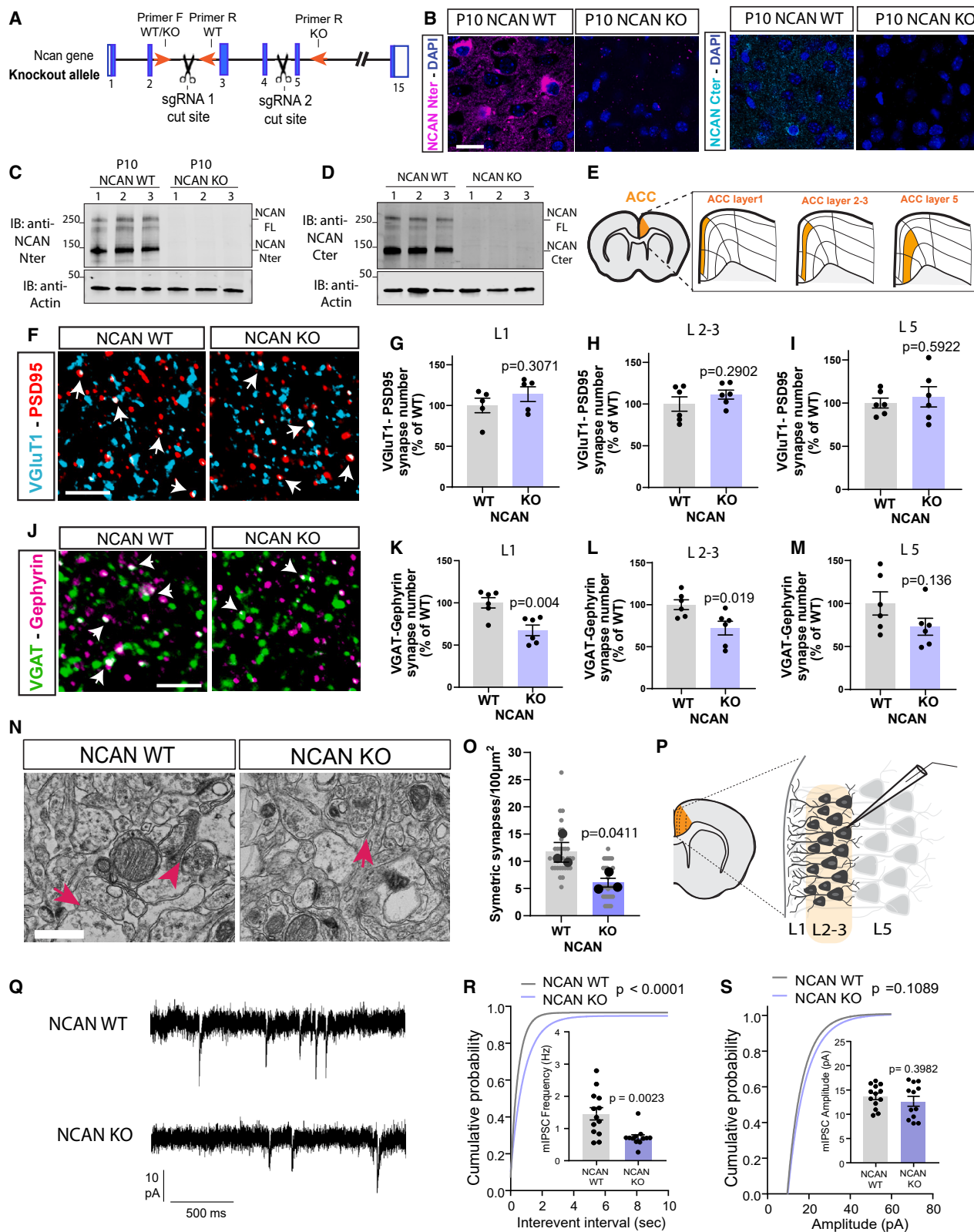
To study NCAN's requirement for synapse development *in vivo*, we analyzed the density of excitatory and inhibitory synapse structures in the ACC of P30 NCAN WT and KO mice (Figure 3E). We identified excitatory synapses by the apposition of *VGluT1* with *PSD95* and inhibitory synapses by the apposition of *VGAT* and *gephyrin* (Figures 3F and 3J). We found no differences in excitatory synapse density between NCAN WT and KO (Figures 3G–3I and S4A–S4C). However, we found a significant reduction in the density of inhibitory synapses (~30%) in NCAN KO mice compared with the WT (Figures 3J–3M and S4D–S4F), with no sex-specific effects observed (Figure S4G).

To confirm these histological findings at the ultrastructural level, we performed electron microscopy (EM) and counted symmetric synapse density in the ACCs of littermate P30 WT and KO mice. We found that NCAN KO mice present a ~50% reduction in inhibitory synapse numbers compared with WT littermates (Figures 3N and 3O). These findings show that NCAN is essential for inhibitory synaptogenesis *in vivo*.

Moreover, we investigated whether NCAN loss affects inhibitory synapse function. We performed whole-cell patch-clamp recordings of miniature inhibitory post-synaptic currents (mIPSCs) from L2-3 pyramidal neurons in the ACC, using acute brain slices of P30 NCAN WT and KO mice (Figure 3P). We found a significant decrease (~50%) in the frequency of mIPSCs in NCAN KO mice compared with WT littermates, with no change in the mean amplitudes (Figures 3Q–3S). These results show that NCAN is required for proper inhibitory synapse formation and function *in vivo*.

Figure 2. NCAN is expressed by astrocytes and is processed into N- and C-terminal fragments

- (A) Detection of *Ncan* in cortical astrocytes. Scale bar 30 μm.
- (B) Quantification of *Ncan* total and astrocytic abundance at P7, P14, P21, and P30, in L1, L2-3, and L5 of the ACC. 6 images/layer/mice. 3 mice for each time point. Data are mean ± S.E.M. One-way ANOVA, Dunnett's post-test.
- (C) Schematic of NCAN full-length and N-terminal and C-terminal fragments. Antibody epitopes are marked for each fragment.
- (D and E) Western blot of NCAN N- and C-terminal expression in cortical lysates.
- (F) Western blot of NCAN N- and C-terminal expression in ACM.
- (G) Staining of NCAN N- and C-terminal in the ACC of P7 *Aldh1L1-GFP* mice. Scale bars, 30 μm. Insert scale bars, 5 μm.
- (H) Staining of NCAN N- and C-terminal in the ECM at P7 and P30. Scale bars, 15 μm.
- (I) STED image of NCAN N-terminal and C-terminal at PNNs marked with WFA. Scale bars, 15 μm. Insert scale bars, 10 μm.



(legend on next page)

NCAN C-terminal fragment is necessary and sufficient for inducing inhibitory synapse formation *in vitro*

To interrogate NCAN N- and C-terminal regions' roles in inhibitory synaptogenesis, we produced recombinant proteins. The middle regions of NCAN containing GAG chains were excluded. We produced a recombinant fragment Nter-IL domain (containing the N-terminal Ig-module and Link domains) and a Cter-ELS domain fragment composed of the C-terminal EGF-like domains, Lectin-like domain, and Sushi domain (Figures 4A–4C). The recombinant proteins were expressed by HEK293 cells and purified from the conditioned media by Histidine-tag affinity purification (Figure S5A).

We treated neuronal cultures with Nter-IL or Cter-ELS domain proteins on DIV8 and 11. We fixed the neurons at DIV13 for analysis. We visualized inhibitory synapses as the apposition of bassoon (on VGAT⁺ axons) with gephyrin. Treatment with Nter-IL did not affect inhibitory synaptogenesis or change the densities of bassoon and gephyrin puncta (Figures 4D, 4E, S5B, and S5C). However, the ELS domain strongly induced inhibitory synaptogenesis (Figures 4F and 4G) without altering overall bassoon or gephyrin puncta numbers (Figures S5D and S5E).

To determine whether the synaptogenic effect of NCAN-Cter-ELS is due to pyramidal neuron dendrite growth, we transfected DIV5 neurons with GFP and treated them with NCAN-Cter-ELS domain as shown in Figures 4F and 4G. We fixed the neurons at DIV13 and stained the cultures with MAP-2 (to label the dendritic tree) and VGlut1 (to identify glutamatergic neurons) (Figure S5F). ACM induced neuronal dendrite growth; however, ELS domain treatment did not induce changes in pyramidal neuron arborization *in vitro* (Figures S5G and S5H). These results show that NCAN-ELS domain induces inhibitory synaptogenesis without altering neuronal morphology.

We next analyzed if NCAN KO ACM retains any inhibitory synaptogenic function. First, we validated by western blot that NCAN is absent in NCAN KO ACM (Figure 4H). Second, we quantified inhibitory synapse numbers in glia-free neuronal cultures treated with WT or NCAN KO ACM. We found that NCAN KO ACM synaptogenic effect is reduced compared with the WT ACM (Figures 4I and 4J), indicating that NCAN is necessary,

at least in part, for ACM-induced inhibitory synaptogenesis *in vitro*. However, reintroducing the NCAN Cter-ELS domain, but not the Nter-IL domain, rescued the inhibitory synaptic deficit of the NCAN KO ACM (Figures 4I and 4J). These results show that NCAN Cter-ELS domain is necessary and sufficient to induce inhibitory synapse formation *in vitro*.

Inhibitory synaptogenesis is impaired in NCAN-ΔELS mutant mice

To analyze the role of NCAN-ELS domain *in vivo*, we designed an NCAN-ΔELS mutant mice using CRISPR-Cas9 system. We targeted exons 9–14 of *Ncan* to remove the EGF-like, Lectin-like, and Sushi domains, leaving the rest of the gene unaltered (Figures 5A and 5B). We validated that NCAN-ΔELS mice express an intact NCAN N-terminal domain but lack the expression of the ELS domain by genomic PCR, immunofluorescence, and western blot (Figures S6A–S6D). Moreover, the localization of NCAN N-terminal at the PNNs is not affected (Figure S6E). Therefore, deleting exons 9–14 in *Ncan* results in a mutant mouse expressing an intact N-terminal fragment but lacking the synaptogenic Cter-ELS domain.

Next, we analyzed whether loss of the Cter-ELS domain alters gross brain morphology. We found no differences in the numbers of inhibitory neurons marked with GAD67 (Figures S6F and S6G) and in the densities of neurons (NeuN⁺), astrocytes (Sox9+/Olig2⁻), or oligodendrocytes (Olig2⁺) between NCAN-ΔELS mutant and WT mice (Figures S6H and S6I). Moreover, the Mendelian distribution of litter genotypes, litter size, survival rate, body weight, and brain density were similar between both genotypes (Figures S6J–S6N). Therefore, deleting NCAN-ELS domain does not cause gross changes in animal survival or the distribution and numbers of neural cell types.

To determine NCAN Cter-ELS domain's role during synapse formation *in vivo*, we quantified the densities of excitatory and inhibitory synapses in the ACC of P30 WT and NCAN-ΔELS mice (Figures 5C–5F, S7A, and S7D). We found no changes in the density of excitatory synapses (Figures 5C and 5D) but a marked decrease (~30%) in the density of inhibitory synapses in NCAN-ΔELS mutant compared with WT (Figures 5E, 5F, and S7D). VGlut1, PSD95, VGAT, or gephyrin puncta numbers

Figure 3. NCAN loss impairs inhibitory synapse formation and function *in vivo*

- (A) Strategy to delete exons 3–4 in *Ncan*.
- (B) NCAN N- and C-terminal staining in P10 ACC of NCAN WT and KO mice. Scale bars, 30 μm.
- (C and D) Western blot of NCAN in cortical lysates from P10 NCAN WT and KO mice.
- (E) Schematic of L1, 2–3, and 5 in the ACC.
- (F) Excitatory synapses in ACC L5 of NCAN WT and KO mice. White arrows indicate excitatory synapses. Scale bar, 10 μm.
- (G, H, and I) Quantification of excitatory synapse numbers in NCAN WT and KO, normalized to the mean of WT. 5 images/section, 3 sections/mouse, and 6 sex-matched littermate pairs. Data points represent mouse averages. Bars are mean ± S.E.M. Unpaired two-tailed t test.
- (J) Inhibitory synapses in L2–3 of NCAN WT and KO mice. Scale bar, 10 μm.
- (K, L, and M) Quantification of inhibitory synapse numbers in NCAN WT and KO, normalized to the mean of WT. 5 images/section, 3 sections/mouse, and 6 sex-matched littermate pairs. Data points represent mouse averages. Bars are mean ± S.E.M. Unpaired two-tailed t test.
- (N) EM images from NCAN WT and KO mice. Scale bars, 2 μm.
- (O) Quantification of inhibitory synapses in NCAN WT and KO mice. 10 images/mouse, 3 sex-matched littermate pairs. Bars are mean ± S.E.M. Unpaired two-tailed t test.
- (P) Scheme of electrophysiology recordings in the ACC.
- (Q) mIPSC traces from NCAN WT and KO mice.
- (R) Quantification of frequency average and cumulative probability of mIPSC from NCAN WT and KO neurons. n = 13 WT and 12 KO neurons. 4 mice/genotype. Kolmogorov-Smirnov test. Unpaired two-tailed t test.
- (S) Quantification of amplitude and cumulative probability from NCAN WT and KO neurons. n = 13 WT and 12 KO neurons. 4 mice/genotype. Kolmogorov-Smirnov test. Unpaired t test. Data are presented as mean ± S.E.M.

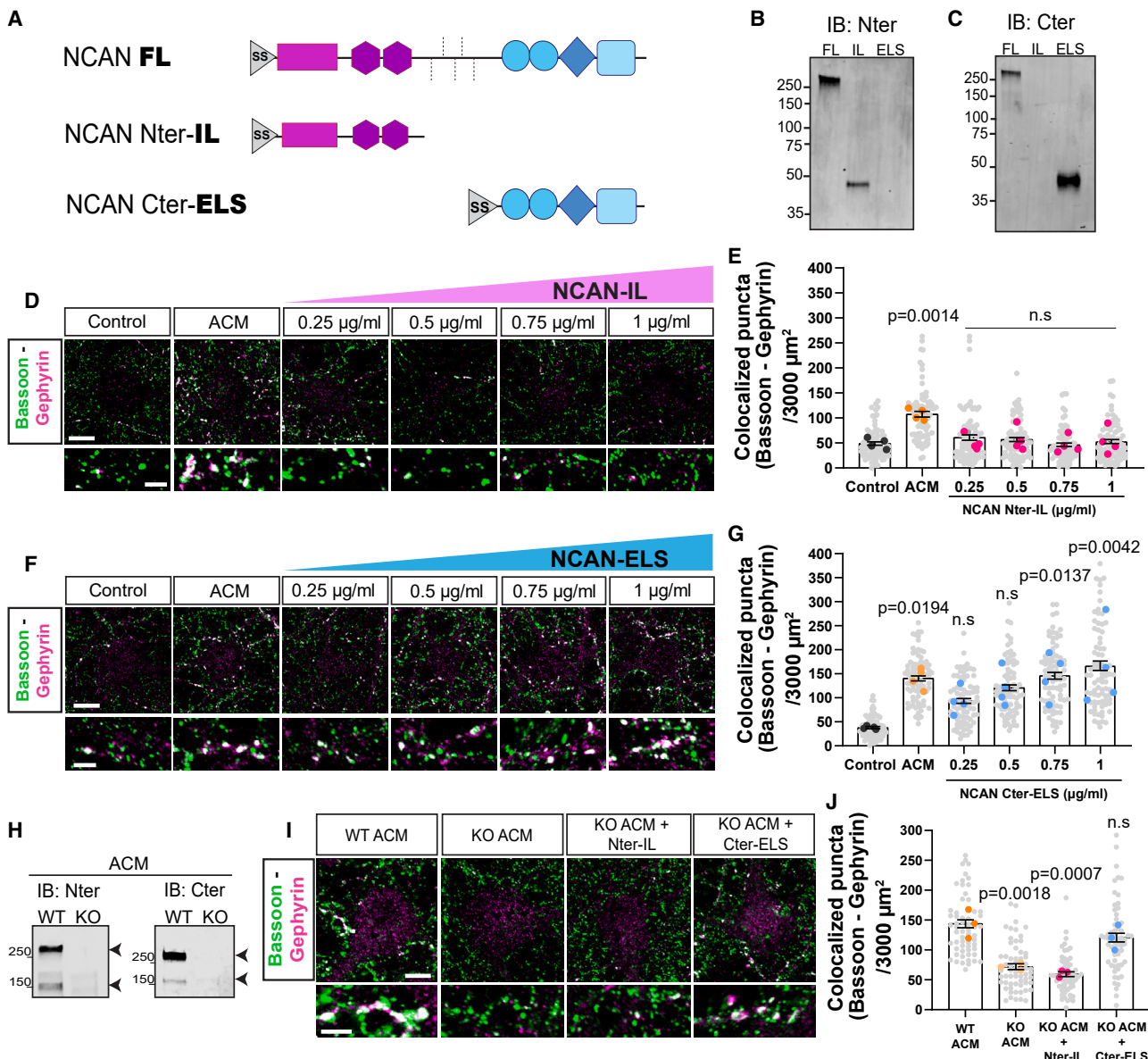


Figure 4. NCAN C-terminal is synaptogenic *in vitro*

(A) Scheme of NCAN full-length (FL), N-terminal-IL (IL) and C-terminal-ELS (ELS) recombinant proteins. SS: secretion signal.

(B and C) Western blot of NCAN-FL, IL and ELS recombinant proteins.

(D) Dose-response curve of NCAN-IL. Bassoon and gephyrin mark inhibitory synapses. Scale bars, 15 µm. Insert scale bars, 5 µm.

(E) Quantification of inhibitory synapses in (D). Data are mean ± S.E.M. n = 4 independent experiments, 20 cells/condition/experiment. One-way ANOVA, Dunnett's post-test.

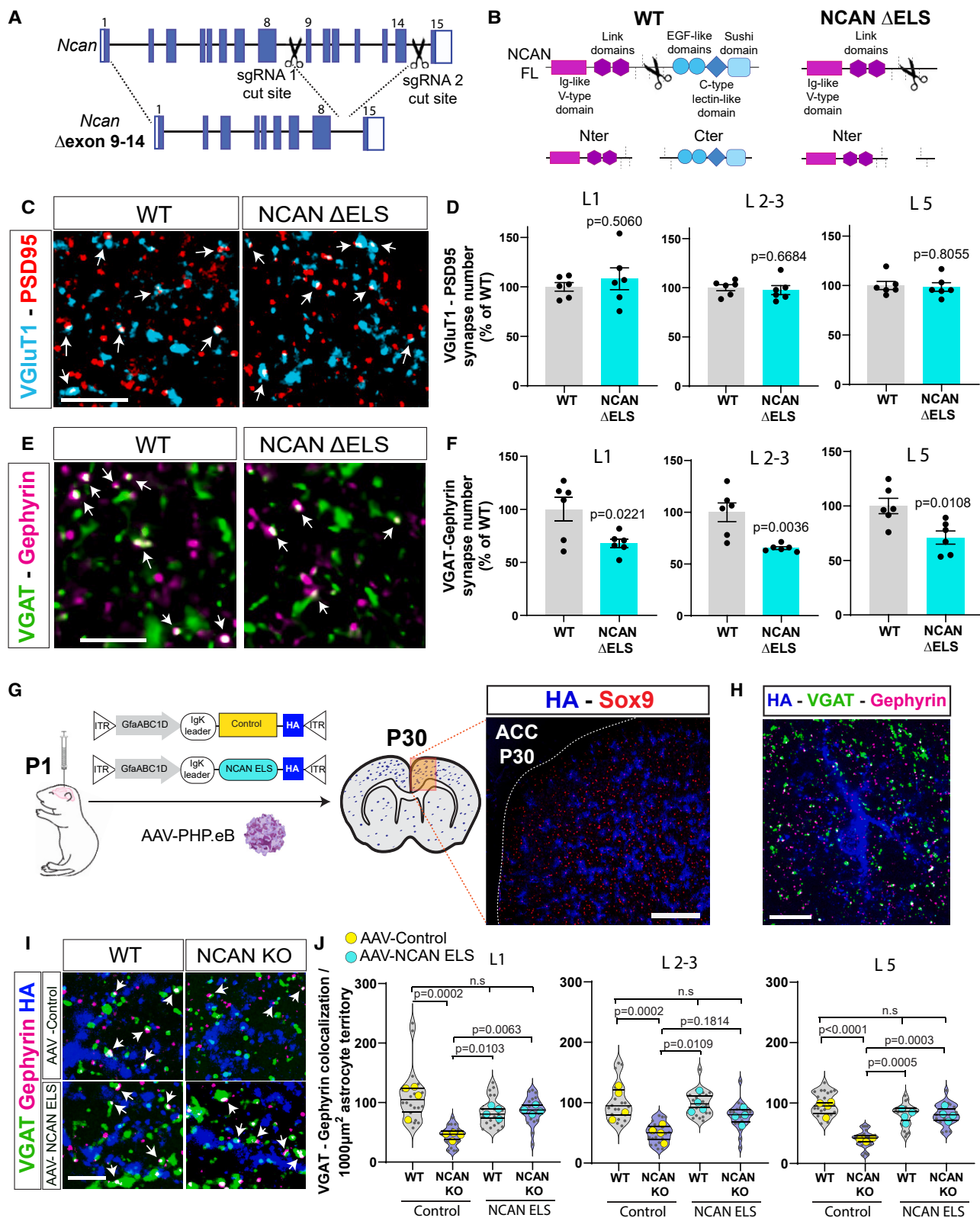
(F) Dose-response curve of NCAN-ELS. Bassoon and gephyrin mark inhibitory synapses. Scale bars, 15 µm. Insert scale bars, 5 µm.

(G) Quantification of inhibitory synapses in (F). Data are mean ± S.E.M. n = 4 independent experiments, 20 cells/condition/experiment. One-way ANOVA, Dunnett's post-test.

(H) Western blot of NCAN N- and C-terminal in NCAN WT and KO ACM.

(I) Rescue experiment with NCAN WT ACM, KO ACM, and recombinant proteins. Bassoon and gephyrin mark inhibitory synapses. Scale bars, 15 µm. Insert scale bars, 5 µm.

(J) Quantification of inhibitory synapses in (I). Data are mean ± S.E.M. n = 3 independent experiments, 20 cells/condition/experiment. One-way ANOVA, Dunnett's post-test.



(legend on next page)

were not different between genotypes (Figures S7B, S7C, S7E, and S7F). These results show that the NCAN-ELS domain is required for inhibitory synapse formation *in vivo*.

To determine if NCAN-ELS domain can rescue the inhibitory synaptic deficits in NCAN KO mice, we designed an AAV viral approach to selectively express HA-tagged NCAN-ELS in astrocytes (GfaABC1D promoter⁴⁴). As a negative control, we used an AAV expressing a secreted protein (IgK-TurboID-HA), with a similar molecular weight as NCAN-ELS (~ 50 KDa). We intracortically injected the AAVs in P1 NCAN WT and KO mice, harvested the brains at P30 (Figure 5G), and analyzed inhibitory synapse density within the territory of transduced astrocytes (Figures 5H, S8A, and S8B). Expression of NCAN-ELS domain in NCAN KO astrocytes *in vivo* was sufficient to restore inhibitory synapse numbers (Figures 5I and 5J). These results show that astrocyte-secreted NCAN C-terminal-ELS domain is necessary and sufficient to induce inhibitory synaptogenesis *in vivo*.

NCAN-ELS domain interacts with excitatory and inhibitory synaptic proteins

NCAN-ELS domain contains protein-protein interaction motifs commonly associated with cell adhesion^{45–47}; therefore, we analyzed whether NCAN C-terminal localizes at synaptic contacts. Using STED, we found that NCAN C-terminal colocalizes with 75% of inhibitory synapses and 40% of excitatory synapses (Figures 6A–6D). The NCAN N-terminal fragment is less abundant at inhibitory synapses (Figures S9A and S9B).

To identify the extracellular binding partners of NCAN-ELS domain, we used *in vivo* proximity labeling by TurboID, a fast, reliable, and non-toxic approach for labeling endogenous interacting proteins.^{48–54} So far, this approach has been mostly utilized to identify the interactome of intracellular proteins.^{49,53} To apply this strategy to NCAN, we virally expressed in astrocytes (GfaABC1D promoter) a secreted version of the TurboID fused to NCAN-Cter-ELS or NCAN-Nter-IL domains (Figures 6E and 6F). To control for unspecific intracellular labeling, we expressed cytosolic-TurboID. To eliminate the interactions of NCAN domains within the secretory pathway and ECM, we expressed a secreted IgK-TurboID (Figures 6E and 6F). These viruses were tested *in vitro* for their ability to be expressed in astrocytes and secrete the NCAN fragments to the ACM and biotinylate proteins (Figures S9C and S9D).

Each virus was intracranially injected into the cerebral cortices of P1 WT mice to identify NCAN interaction partners during the

peak of synaptogenesis. Between P18-P20, mice received biotin injections, and at P21, the cortices were collected (Figure S9E). This experimental design allowed for the broad expression of the TurboID constructs in astrocytes resulting in abundant biotinylation (Figure S9F). Biotinylated proteins were purified from cortical lysates for proteomic analysis (Figure S9G).

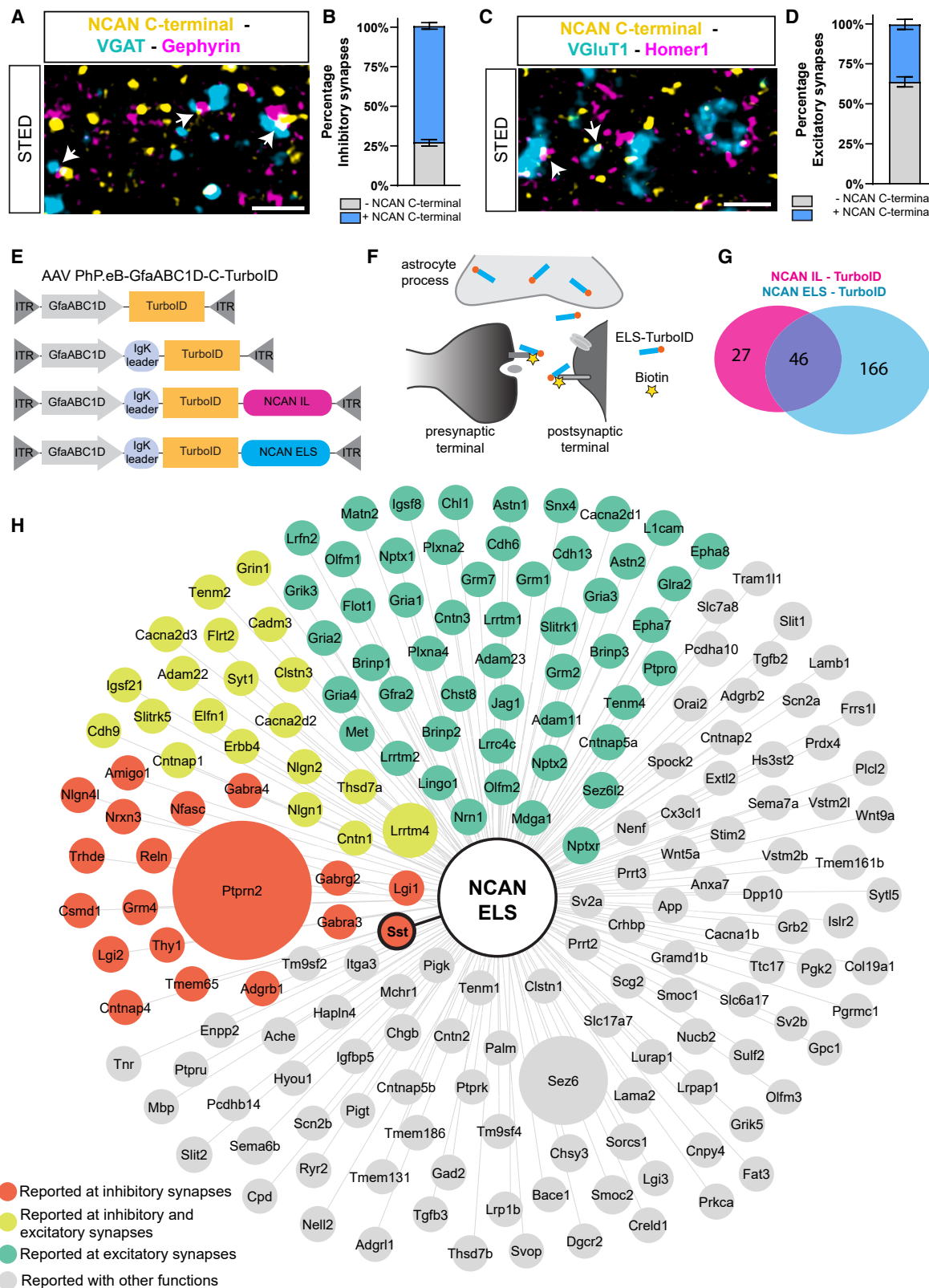
Biotinylated proteins were analyzed by quantitative high-resolution liquid chromatography-tandem mass spectrometry (LC-MS/MS).^{49,51} 4726 unique proteins were identified (Table S1). Compared with secreted IgK-TurboID and Cytosolic-TurboID controls, we found 27 and 166 unique membrane and secreted proteins significantly enriched (>1.5-fold) in NCAN Nter-IL-TurboID and NCAN Cter-ELS-TurboID fractions, respectively (Figure 6G). Moreover, we found 46 shared proteins between Nter-IL-TurboID and Cter-ELS-TurboID (Figure 6G; Table S2). We filtered these proteomic lists for known interactors and found several interacting proteins present at PNNs (Figure S9H). To analyze if the Cter-ELS-TurboID interactome contains known synaptic proteins, we combined the 166 unique Cter-ELS-TurboID interactors and 46 shared Nter-IL-TurboID and Cter-ELS-TurboID proteins (Figure 6H; Tables S2 and S3) and cross-referenced it with a cell-type-specific RNA expression database from the mouse cortex.³¹ We found that most of these proteins are highly expressed in neurons (Table S4). This final proteomic list includes known synaptic proteins from excitatory synapses and proteins present at inhibitory synapses, such as the leucine-rich secreted protein Lgi1/2 and GABA receptors (Gabra3 and 4) (Figure 6H). Interestingly, NCAN-ELS is proximal to the neuropeptide SST.⁵⁵ These results revealed that in the extracellular matrix NCAN-IL and -ELS interactome diverge, and NCAN-ELS interacts with multiple synaptic proteins. Because NCAN-ELS is proximal to SST, we next investigated if NCAN C-terminal fragment controls the formation of distinct inhibitory synaptic circuits.

NCAN C-terminal controls SST+ synapse formation and function

To study if NCAN C-terminal differentially localizes to SST+ or PV+ synapses, we labeled P30 ACC brain sections with SST (presynaptic) and gephyrin and PV+ synapses with presynaptic marker Synaptotagmin2 (Syt2), which labels axo-somatic PV+ synapses from basket cells onto neuronal bodies,^{6,56} together with gephyrin (Figure 7A). We chose Syt2+ because basket cells are the most abundant type of PV+ interneuron in the

Figure 5. Inhibitory synaptogenesis is impaired in NCAN ΔELS mutant mice

- (A) Strategy to delete exons 9–14 from *Ncan*.
- (B) Scheme of NCAN WT protein and NCAN ΔELS mutant.
- (C) Excitatory synapses in ACC L5 of NCAN WT and ΔELS mice. Scale bar, 10 μm.
- (D) Quantification of excitatory synapse in NCAN WT and ΔELS mutants, normalized to the mean of WT in L1, L2-3, and L5. 5 images/section, 3 sections/mouse, and 6 sex-matched littermate pairs. Data points represent mouse averages. Bars are mean ± S.E.M. Unpaired two-tailed t test.
- (E) Inhibitory synapses in ACC L1 of NCAN WT and ΔELS mice. Scale bar, 10 μm.
- (F) Quantification of inhibitory synapse numbers in NCAN WT and ΔELS, normalized to the mean of WT in L1, L2-3, and L5. 5 images/section, 3 sections/mouse, and 6 sex-matched littermate pairs. Bars are mean ± S.E.M. Unpaired two-tailed t test.
- (G) Strategy used for rescue experiment *in vivo*. Scale bars, 150 μm.
- (H) Inhibitory synapses inside astrocyte territory. Scale bars, 40 μm.
- (I) Inhibitory synapses within astrocyte territory in L1 of NCAN WT and KO mice transduced with AAV-Control or AAV-NCAN-ELS. Scale bar, 10 μm.
- (J) Quantification of the density of inhibitory synapses in (I). 5 astrocytes/mouse, 4 mice for each condition. Bars are mean ± S.E.M. One-way ANOVA, Tukey's post-test.



(legend on next page)

neocortex.^{2,57} We found that 50% of SST+ synapses colocalize with NCAN C-terminal, whereas only 25% of Syt2+ synapses colocalize with this fragment (Figures 7B–7E), indicating that the C-terminal domain is more frequently found at SST+ synaptic contacts.

To study if NCAN-ELS induces the formation of different inhibitory synapse subtypes *in vitro*, we treated neuronal cultures with recombinant NCAN-Cter-ELS protein (Figures 7F and 7I). Although the ACM increased both SST+ and Syt2+ synapse numbers, NCAN-Cter-ELS only induced SST+ synaptogenesis (Figures 7G and 7J). NCAN-Cter-ELS did not increase Syt2 or SST+ presynaptic puncta numbers *in vitro*. However, the ACM treatment caused a significant increase in SST+ and Syt2 puncta (Figures 7H and 7K), indicating that ACM may contain additional factors controlling inhibitory synapse formation.

Next, we analyzed if NCAN-ELS domain loss affects SST+ synaptogenesis *in vivo*. We found that SST+ inhibitory synapses were significantly reduced between P30 ACC NCAN-ΔELS and WT mice (Figures 7L and 7M). We observed reduced SST+ puncta in L2–3 of NCAN ΔELS mice (Figure 7N). These changes in SST+ synapses were not due to SST+ neuronal loss (Figures 7O–7Q). There were no differences in perisomatic Syt2+ synapse numbers around neuronal cell bodies (NeuN+) between NCAN-ΔELS and WT mice (Figures S10A–S10C). However, in the L2–3 neuropil of NCAN-ΔELS mice, we found a significant reduction of Syt2+ synapses (Figures S10F and S10G). Interestingly, Syt2 puncta and PV+ neuronal number were not affected in the ACC of NCAN-ΔELS and WT mice (Figures S10D, S10E, and S10H–S10K). Together, these results show that NCAN-ELS domain is crucial for the development of SST+ inhibitory synapses in the ACC.

By using the same viral rescue strategy as described in Figure 5G, we tested if NCAN C-terminal-ELS can rescue SST+ synapse numbers in NCAN KO mice. We quantified the number of SST+ synapses within the territories of the transduced astrocytes (Figure 7R). We found that at P30 NCAN, ELS domain rescued SST+ synaptic density in the territory of NCAN KO astrocytes to similar levels as in WT mice (Figure 7S), without affecting Syt2+ perisomatic inhibitory synapses (Figures S10L–S10N). Taken together, these results show that NCAN C-terminal-ELS domain is necessary and sufficient for the development of SST+ synapses in the ACC.

Finally, we investigated how NCAN-ELS domain loss impacts excitatory and inhibitory synaptic function. We recorded miniature excitatory post-synaptic current (mEPSC) and mIPSCs from L2–3 pyramidal neurons in the ACC in P30 NCAN-ΔELS mutant or WT mice (Figures 8A and S11A). We found that the

mEPSC amplitude and frequency (Figures S11B–S11E) and the mIPSC amplitude was similar between genotypes (Figures 8B and 8C). However, the frequency of mIPSCs in the NCAN-ΔELS mutant was significantly reduced (~35%) compared with WT mice (Figures 8D and 8E). *In vivo*, SST+ synapses are formed mostly on the distal dendrites of pyramidal neurons, while PV+ synapses are formed mainly in the perisomatic domain.^{58,59} We analyzed the recording data to determine if the reduction in mIPSC frequency in the mutant mice is due to the loss of perisomatic or distal dendritic synaptic events. To do so, we took advantage of the rise time difference between perisomatic (fast) and dendritic (slow) inhibition and analyzed the rise time of mIPSCs in WT and NCAN-ΔELS mutant mice^{60,61} (Figure 8F). We observed a decrease (~28%) in the 10%–90% rise times of the mIPSCs in NCAN-ΔELS mutant mice (Figure 8G). We then classified fast mIPSCs (perisomatic events: < 2.8 ms) and slow mIPSCs (distal dendritic events: >2.8 ms). We found no change in the amplitudes of fast or slow mIPSCs (Figure 8H) but found a significant decrease (~64%) in the frequency of slow mIPSCs in NCAN-ΔELS mutants (Figure 8I). These results strongly suggest that the NCAN-ELS domain controls the formation and function of dendrite-targeting inhibitory synapses, which are often formed by the SST+ interneuron contacts. Altogether, our findings reveal a mechanism through which astrocytes control circuit-specific inhibitory synapse formation in the developing cortex.

DISCUSSION

Astrocytes control inhibitory synaptogenesis

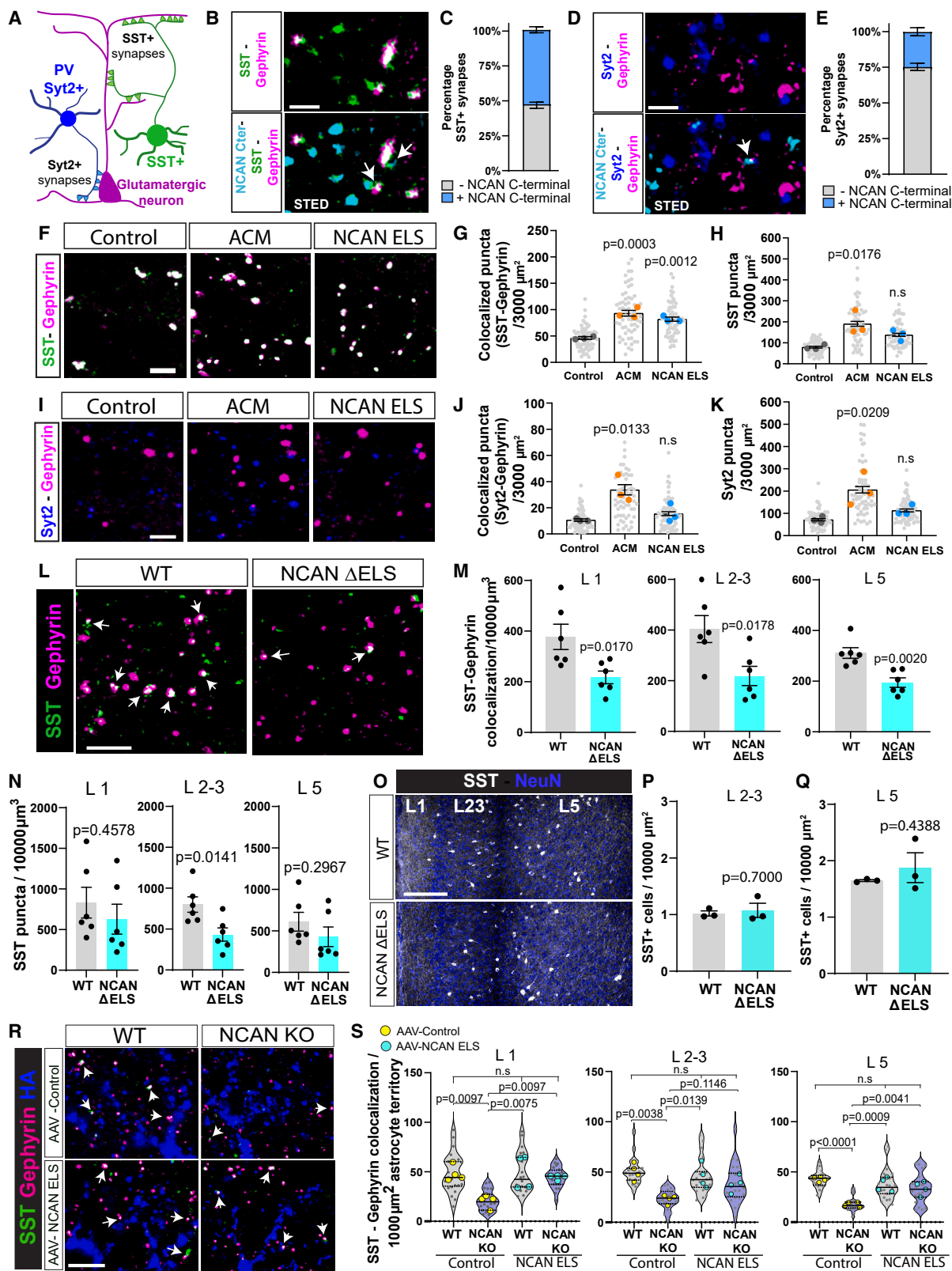
Astrocytes powerfully influence the formation and maturation of excitatory and inhibitory synapses through secreted synaptogenic factors and cell adhesion proteins.^{10–13,40,62–65} For example, astrocyte-neuron contacts established through adhesion protein NrCAM regulate inhibitory synapse formation.⁵¹ However, the identity of the astrocyte-secreted signals controlling inhibition in the CNS is less understood. Here, we show that astrocyte-secreted NCAN controls inhibitory synaptogenesis and function. Our results highlight the importance of astrocyte-secreted molecules in controlling excitatory/inhibitory synaptic balance and brain connectivity.

NCAN proteolytic processing and function

NCAN undergoes a proteolytic cleavage that occurs during a developmental period coinciding with synaptogenesis. It is thought that NCAN is cleaved between amino acids 638 and 639.²² Yet, the functional relevance of this cleavage during

Figure 6. NCAN-ELS domain interactome contains proteins enriched at excitatory and inhibitory synapses

- (A) STED image of NCAN C-terminal, VGAT, and gephyrin in P30 WT mice, ACC L2–3. Scale bars, 1 μm.
- (B) Percentage of NCAN C-terminal at inhibitory synapses. 3 sections/mouse, 3 WT mice. Bars are mean ± S.E.M.
- (C) STED image of NCAN C-terminal together, VGlut1, and Homer1 in P30 WT mice, ACC L2–3. Scale bars, 1 μm.
- (D) Percentage of NCAN C-terminal at excitatory synapses. 3 sections/mouse, 3 WT mice. Bars are mean ± S.E.M.
- (E) TurboID constructs. IgK leader: secretion signal.
- (F) TurboID approach.
- (G) Venn diagram of NCAN-IL and ELS extracellular proteome.
- (H) NCAN-ELS-TurboID extracellular proteome.



(legend on next page)

development remains poorly understood. Is NCAN cleavage required for the C-terminal synaptogenic effect? Even though NCAN C-terminal is not enriched at PNNs, a small fraction of NCAN full-length is stored in these structures. Thus, PNNs may function as NCAN C-terminal reservoirs. If NCAN in these structures is protected or available for cleavage during development, how NCAN processing is impacted during injury or disease is still to be determined. Therefore, identifying the molecular and cellular mechanism triggering NCAN processing will be an important topic for future studies.

NCAN C-terminal induces circuit-specific inhibitory synaptogenesis

In the cerebral cortex, the heterogeneity of GABAergic synapses arises from the different interneuron subtypes.^{2,5,6,66} Can astrocytes differentially coordinate the formation of distinct GABAergic synaptic contacts? Our results reveal a mechanism by which astrocytes control SST+ inhibitory synaptogenesis and function through NCAN. However, the ACM induces both SST+ and PV+ synapses, but NCAN C-terminal fragment specifically promotes SST+ synaptogenesis. In agreement, the loss of the NCAN-ELS domain results in a significant reduction of SST+ synapse density *in vivo*. Since disruption of the SST interneuron network in the cortex results in impaired synaptic connectivity of the PV neurons,^{67,68} our results bring forth the question if NCAN C-terminal's effect on SST synapses could indirectly impact the properties of other inhibitory neuronal networks. For example, PV+ synapses mature later in development than SST+ synapses and require a feed-forward circuit with SST+ neurons. Our analysis did not test other types of inhibitory synapses that are made by interneurons such as VIP+, Reelin+, or NPY+ neurons. Those neurons comprise a smaller proportion of interneurons in the cortex; however, they form critical neuronal networks in different

cortical areas and layers.^{66,69,70} Future studies on how astrocytes signal to different interneuron subtypes are needed to determine how these glial cells control GABAergic synaptic diversity.

Role of NCAN in neurological disorders and brain injury

After brain injury or in degenerative disorders, reactive astrocytes undergo morphological and functional changes⁷¹ and strongly upregulate NCAN.^{22,71} Interestingly, TGF-β, which is also upregulated following traumatic brain injury, is known to promote NCAN expression and revert reactive astrocytes to a non-reactive state.⁷¹ Is NCAN expression a downstream mechanism to limit astrocyte reactivity under pathological conditions? Future studies should be done to determine if NCAN N- or C-terminal can be targeted to control reactive astrocytes during injury and disease.

Previous studies in amyotrophic lateral sclerosis (ALS) models showed that diseased motor neurons are surrounded by NCAN.⁷² Moreover, NCAN C-terminal expression in the cerebrospinal fluid of patients with ALS is significantly increased compared with control patients.⁷³ EGF and TGF-β induce NCAN expression and are persistently elevated in ALS.^{22,74} Testing whether NCAN elevation in diseases such as ALS is a protective or pathological mechanism would be an important future direction.

In Rett syndrome, inhibitory synaptic number and synaptic function are altered.^{75,76} Interestingly, Rett mouse model (*Mecp2* knockout) ACM proteomic analysis showed a significant increase in NCAN expression compared to the WT controls.⁷⁷ It would be interesting to determine if decreasing NCAN function would be beneficial in this model. Genetic variations in NCAN are associated with impaired memory and visuospatial skills in humans and are risk factors for BD, SCZ, and major depressive

Figure 7. NCAN C-terminal fragment controls SST synaptogenesis

- (A) Scheme of SST+ and PV Syt2+ targeting glutamatergic neurons.
- (B) STED image of NCAN C-terminal, SST, and gephyrin in P30 WT mice, ACC L2-3. Scale bars, 1 μm.
- (C) Percentage of NCAN C-terminal at SST+ synapses. 3 sections/mouse, 3 WT mice. Bars are mean ± S.E.M.
- (D) STED image of NCAN C-terminal, Syt2, and gephyrin in P30 WT mice, L2-3. Scale bars, 1 μm.
- (E) Percentage of NCAN C-terminal at Syt2+ synapses. 3 sections/mouse, 3 WT mice. Bars are mean ± S.E.M.
- (F) SST+ synapses neuronal cultures treated with control, ACM, or ELS recombinant protein. Scale bars, 5 μm.
- (G) Quantification of SST+ synapses from (F). Data are mean ± S.E.M. n = 3 independent experiments, 20 cells/condition/experiment. One-way ANOVA, Dunnett's post-test.
- (H) Quantification of SST puncta from (F). Data are mean ± S.E.M. n = 3 independent experiments, 20 cells/condition/experiment. One-way ANOVA, Dunnett's post-test.
- (I) Images of Syt2+ synapses in neuronal cultures treated with control, ACM, or ELS recombinant protein. Scale bars, 5 μm.
- (J) Quantification of Syt2+ synapses from (I). Data are mean ± S.E.M. n = 3 independent experiments, 20 cells/condition/experiment. One-way ANOVA, Dunnett's post-test.
- (K) Quantification of Syt2 puncta from F. Data are mean ± S.E.M. n = 3 independent experiments, 20 cells/condition/experiment. One-way ANOVA, Dunnett's post-test.
- (L) SST+ synapses in ACC L1 of NCAN WT and ΔELS mice. Scale bar, 10 μm.
- (M) Quantification of SST+ synapse density in NCAN WT and ΔELS, ACC L1, L2-3, and L5. 5 images/section, 3 sections/mouse, and 6 sex-matched littermate pairs. Bars are mean ± S.E.M. Unpaired two-tailed t test.
- (N) Quantification of SST puncta in NCAN WT and ΔELS, ACC L1, L2-3, and L5. 5 images/section, 3 sections/mouse, and 6 sex-matched littermate pairs. Bars are mean ± S.E.M. Unpaired two-tailed t test.
- (O) SST+ neurons in the ACC of NCAN WT and ΔELS mice. Scale bars, 150 μm.
- (P and Q) Quantification of SST numbers in L2-3 and L5 in NCAN WT and ΔELS mice. 1 image/section, 3 sections/mouse, 3 mice. Bars are mean ± S.E.M. Unpaired two-tailed t test.
- (R) SST+ synapses within astrocyte territory in L1 of NCAN WT and KO mice transduced with AAV-Control or AAV-NCAN-ELS. Scale bar, 10 μm.
- (S) Quantification of the density of SST+ synapses from R. 5 astrocytes/mouse, 4 mice for each condition. Bars are mean ± S.E.M. One-way ANOVA, Tukey's post-test.

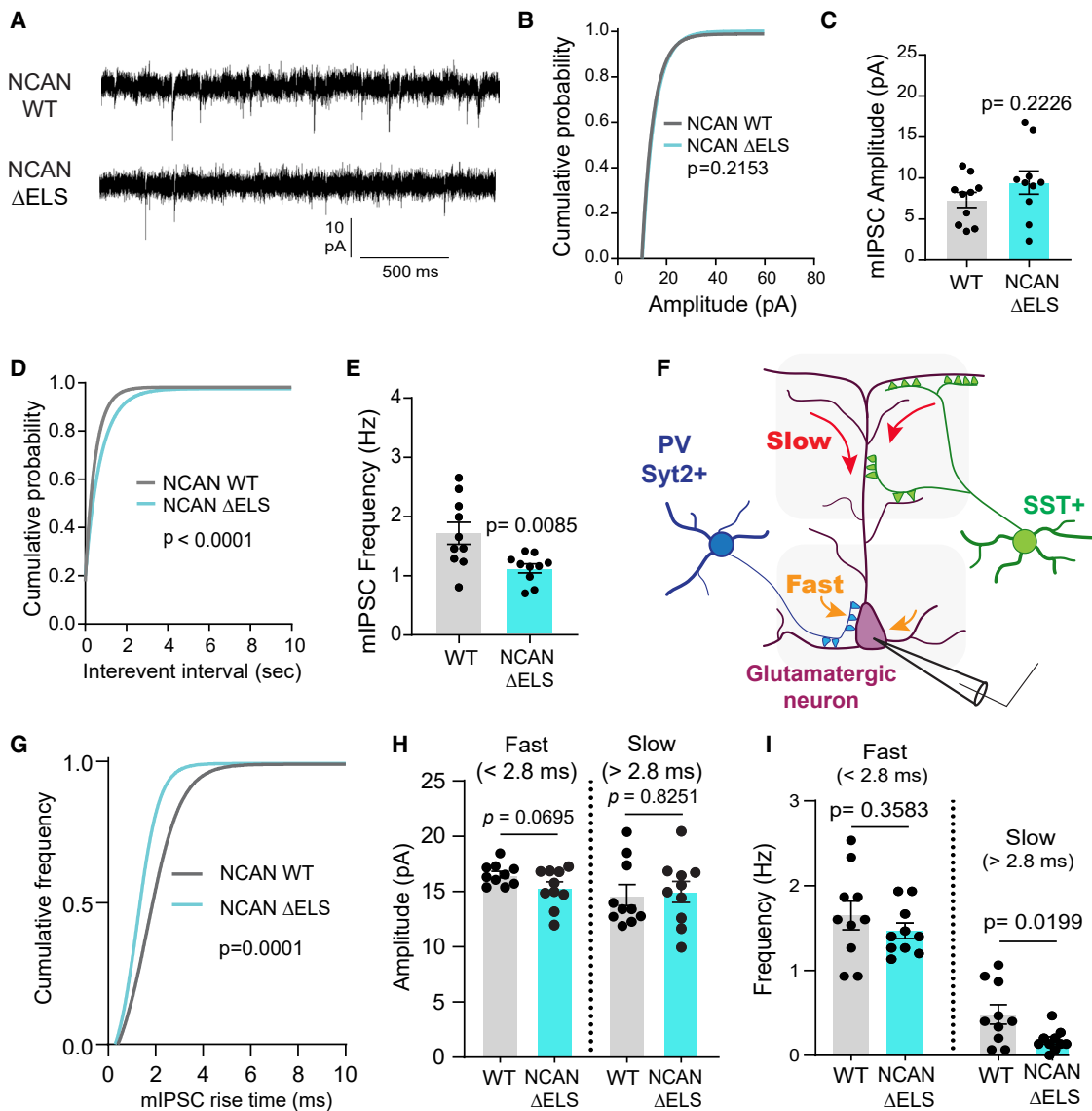


Figure 8. NCAN C-terminal controls inhibitory synaptic function

(A) mIPSC traces from NCAN WT and ΔELS mice.

(B and C) Quantification of amplitude and cumulative probability from NCAN WT and ΔELS mice pyramidal neurons. $n = 10$ WT and 10 ΔELS neurons. 3 mice/genotype. Kolmogorov-Smirnov test. Unpaired t test.

(D and E) Quantification of mIPSC frequency average and cumulative probability from NCAN WT and ΔELS mice pyramidal neurons. $n = 10$ WT and 10 ΔELS neurons. 3 mice/genotype. Kolmogorov-Smirnov test. Unpaired two-tailed t test.

(F) Schematic of somatic and dendritic synaptic inputs on pyramidal neurons.

(G) Quantification of cumulative frequency of mIPSC rise time in P30-35 NCAN WT and ΔELS littermates. $n = 10$ WT and 10 ΔELS neurons. 3 mice/genotype. Kolmogorov-Smirnov test.

(H) Quantification of somatic and dendritic amplitude in P30-35 NCAN WT and ΔELS littermates. $n = 10$ WT and 10 ΔELS neurons. 3 mice/genotype. Unpaired two-tailed t test Data are mean \pm S.E.M.

(I) Frequency of somatic and dendritic events from NCAN WT and ΔELS mutant mice. $n = 10$ WT and 10 KO neurons. 3 mice/genotype. Unpaired two-tailed t test. Data are mean \pm S.E.M.

disorder.^{18,20,33} Noteworthy, the expression of *Sst* mRNA in the prefrontal cortex of subjects with SCZ is reduced compared with control patients,^{78–80} indicating a converging mechanism suggesting a circuit-specific impairment of inhibition in these diseases.

In conclusion, we have identified the astrocyte-secreted NCAN C-terminal fragment as a novel inhibitory synaptogenic protein controlling SST+ synapses and inhibitory synaptic function. It is a promising therapeutic target with potential implications in the pathogenesis of neurological disorders and brain injury.

STAR★METHODS

Detailed methods are provided in the online version of this paper and include the following:

- **KEY RESOURCES TABLE**
- **RESOURCE AVAILABILITY**
 - Lead contact
 - Materials availability
 - Data and code availability
- **EXPERIMENTAL MODEL AND SUBJECT DETAILS**
 - Animals
- **METHOD DETAILS**
 - Primary cultures
 - Cell lines
 - shRNA and cDNA plasmids
 - Immunocytochemistry
 - Multiplexed immunofluorescence and RNA-FISH for simultaneous detection of protein and RNA targets
 - Protein extraction and western blotting
 - Adeno-associated virus (AAV) production and administration
 - Proteomic analysis
 - Electrophysiology
 - Transmission electron microscopy
- **QUANTIFICATION AND STATISTICAL ANALYSIS**
 - SynBot software
 - Macro for synapse analysis around cell soma
 - Macro for area of colocalization smRNA FISH

SUPPLEMENTAL INFORMATION

Supplemental information can be found online at <https://doi.org/10.1016/j.neuron.2024.03.007>.

ACKNOWLEDGMENTS

This work was supported by a Holland-Trice Brain Research Award and the National Institutes of Health grants to C.E. U19NS123719 and R01NS102237. D.I. and S.W. were supported by fellowships from the Foerster-Bernstein Family and D.I. by the Pew Charitable Trust Latin American Fellows Program in the Biomedical Sciences. K.S. was supported by an NRSA from NINDS F32NS112565. F.P.U.S. was supported by a fellowship from the Regeneration Next Initiative and the Ramon y Cajal Young Investigator Award (RYC2021-033202-I). J.S. was supported by an NRSA from NINDS 1F31NS134252-01. We thank the Eroglu lab, Dr. Scott Soderling, Dr. Debra Silver, Dr. Nicola Allen, Dr. Staci Bilbo, and Dr. Jeremy Kay for the valuable feedback and Duke's Light Microscopy Core Facility, Transgenic Mouse Facility, Electron Microscopy Service Core Facility, Proteomics, and Metabolomics Core Facility, and Viral Vector Core Facility. C.E. is an HHMI investigator.

AUTHOR CONTRIBUTIONS

Conceptualization, D.I. and C.E.; methodology, D.I., S.W., K.S., F.P.U.S., and C.E.; investigation, D.I., S.W., K.S., F.P.U.S., L.N., and D.S.B; formal analysis, D.I., S.W., K.S., F.P.U.S., and L.N.; software design, J.S; writing original draft, D.I. and C.E.; writing review/editing, D.I., S.W., K.S., F.P.U.S., L.N., D.S.B., J.S., and C.E.; funding acquisition, D.I. and C.E.

DECLARATION OF INTERESTS

The authors declare no competing interests.

Received: April 18, 2023

Revised: January 22, 2024

Accepted: March 7, 2024

Published: April 3, 2024

REFERENCES

1. Froemke, R.C. (2015). Plasticity of cortical excitatory-inhibitory balance. *Annu. Rev. Neurosci.* 38, 195–219. <https://doi.org/10.1146/annurev-neuro-071714-034002>.
2. Lim, L., Mi, D., Llorca, A., and Marín, O. (2018). Development and functional diversification of cortical interneurons. *Neuron* 100, 294–313. <https://doi.org/10.1016/j.neuron.2018.10.009>.
3. Favuzzi, E., and Rico, B. (2018). Molecular diversity underlying cortical excitatory and inhibitory synapse development. *Curr. Opin. Neurobiol.* 53, 8–15. <https://doi.org/10.1016/j.conb.2018.03.011>.
4. Bartolini, G., Ciceri, G., and Marín, O. (2013). Integration of GABAergic interneurons into cortical cell assemblies: lessons from embryos and adults. *Neuron* 79, 849–864. <https://doi.org/10.1016/j.neuron.2013.08.014>.
5. Kepecs, A., and Fishell, G. (2014). Interneuron cell types are fit to function. *Nature* 505, 318–326. <https://doi.org/10.1038/nature12983>.
6. Favuzzi, E., Deogracias, R., Marques-Smith, A., Maeso, P., Jezequel, J., Exposito-Alonso, D., Balia, M., Kroon, T., Hinojosa, A.J., F Maraver, E., et al. (2019). Distinct molecular programs regulate synapse specificity in cortical inhibitory circuits. *Science* 363, 413–417. <https://doi.org/10.1126/science.aau8977>.
7. Sancho, L., Contreras, M., and Allen, N.J. (2021). Glia as sculptors of synaptic plasticity. *Neurosci. Res.* 167, 17–29. <https://doi.org/10.1016/j.neures.2020.11.005>.
8. Eroglu, C., and Barres, B.A. (2010). Regulation of synaptic connectivity by glia. *Nature* 468, 223–231. <https://doi.org/10.1038/nature09612>.
9. Perea, G., Navarrete, M., and Araque, A. (2009). Tripartite synapses: astrocytes process and control synaptic information. *Trends Neurosci.* 32, 421–431. <https://doi.org/10.1016/j.tins.2009.05.001>.
10. Christopherson, K.S., Ullian, E.M., Stokes, C.C., Mullowney, C.E., Hell, J.W., Agah, A., Lawler, J., Mosher, D.F., Bernstein, P., and Barres, B.A. (2005). Thrombospondins are astrocyte-secreted proteins that promote CNS synaptogenesis. *Cell* 120, 421–433. <https://doi.org/10.1016/j.cell.2004.12.020>.
11. Kucukdereli, H., Allen, N.J., Lee, A.T., Feng, A., Ozlu, M.I., Conatser, L.M., Chakraborty, C., Workman, G., Weaver, M., Sage, E.H., et al. (2011). Control of excitatory CNS synaptogenesis by astrocyte-secreted proteins Hevin and SPARC. *Proc. Natl. Acad. Sci. USA.* 108, E440–E449. <https://doi.org/10.1073/pnas.1104977108>.
12. Allen, N.J., Bennett, M.L., Foo, L.C., Wang, G.X., Chakraborty, C., Smith, S.J., and Barres, B.A. (2012). Astrocyte glycans 4 and 6 promote formation of excitatory synapses via GluA1 AMPA receptors. *Nature* 486, 410–414. <https://doi.org/10.1038/nature11059>.
13. Blanco-Suarez, E., Liu, T.F., Kopelevich, A., and Allen, N.J. (2018). Astrocyte-secreted chordin-like 1 drives synapse maturation and limits plasticity by increasing synaptic GluA2 AMPA receptors. *Neuron* 100, 1116–1132.e13. <https://doi.org/10.1016/j.neuron.2018.09.043>.
14. Elmariah, S.B., Oh, E.J., Hughes, E.G., and Balice-Gordon, R.J. (2005). Astrocytes regulate inhibitory synapse formation via Trk-mediated modulation of postsynaptic GABA_A receptors. *J. Neurosci.* 25, 3638–3650. <https://doi.org/10.1523/JNEUROSCI.3980-04.2005>.
15. Hughes, E.G., Elmariah, S.B., and Balice-Gordon, R.J. (2010). Astrocyte secreted proteins selectively increase hippocampal GABAergic axon length, branching, and synaptogenesis. *Mol. Cell. Neurosci.* 43, 136–145. <https://doi.org/10.1016/j.mcn.2009.10.004>.
16. Reichelt, A.C., Hare, D.J., Bussey, T.J., and Saksida, L.M. (2019). Perineuronal nets: plasticity, protection, and therapeutic potential. *Trends Neurosci.* 42, 458–470. <https://doi.org/10.1016/j.tins.2019.04.003>.

17. Schmidt, S., Arendt, T., Morawski, M., and Sonntag, M. (2020). Neurocan contributes to perineuronal net development. *Neuroscience* 442, 69–86. <https://doi.org/10.1016/j.neuroscience.2020.06.040>.
18. Wang, P., Cai, J., Ni, J., Zhang, J., Tang, W., and Zhang, C. (2016). The NCAN gene: schizophrenia susceptibility and cognitive dysfunction. *Neuropsychiatr. Dis. Treat.* 12, 2875–2883. <https://doi.org/10.2147/NDT.S118160>.
19. Schultz, C.C., Mühlleisen, T.W., Nenadic, I., Koch, K., Wagner, G., Schachtzabel, C., Siedek, F., Nöthen, M.M., Rietschel, M., Deufel, T., et al. (2014). Common variation in NCAN, a risk factor for bipolar disorder and schizophrenia, influences local cortical folding in schizophrenia. *Psychol. Med.* 44, 811–820. <https://doi.org/10.1017/S0033291713001414>.
20. Raum, H., Dietsche, B., Nagels, A., Witt, S.H., Rietschel, M., Kircher, T., and Krug, A. (2015). A genome-wide supported psychiatric risk variant in NCAN influences brain function and cognitive performance in healthy subjects. *Hum. Brain Mapp.* 36, 378–390. <https://doi.org/10.1002/hbm.22635>.
21. Miró, X., Meier, S., Dreisow, M.L., Frank, J., Strohmaier, J., Breuer, R., Schmäl, C., Albayram, Ö., Pardo-Olmedilla, M.T., Mühlleisen, T.W., et al. (2012). Studies in humans and mice implicate neurocan in the etiology of mania. *Am. J. Psychiatry* 169, 982–990. <https://doi.org/10.1176/appi.ajp.2012.11101585>.
22. Asher, R.A., Morgenstern, D.A., Fidler, P.S., Adcock, K.H., Oohira, A., Braisted, J.E., Levine, J.M., Margolis, R.U., Rogers, J.H., and Fawcett, J.W. (2000). Neurocan is upregulated in injured brain and in cytokine-treated astrocytes. *J. Neurosci.* 20, 2427–2438. <https://doi.org/10.1523/JNEUROSCI.20-07-02427.2000>.
23. Retzler, C., Göhring, W., and Rauch, U. (1996). Analysis of neurocan structures interacting with the neural cell adhesion molecule N-CAM. *J. Biol. Chem.* 271, 27304–27310. <https://doi.org/10.1074/jbc.271.44.27304>.
24. Deepa, S.S., Carulli, D., Galtrey, C., Rhodes, K., Fukuda, J., Mikami, T., Sugahara, K., and Fawcett, J.W. (2006). Composition of perineuronal net extracellular matrix in rat brain: a different disaccharide composition for the net-associated proteoglycans. *J. Biol. Chem.* 281, 17789–17800. <https://doi.org/10.1074/jbc.M600544200>.
25. Mohan, V., Wyatt, E.V., Gotthard, I., Phend, K.D., Diestel, S., Duncan, B.W., Weinberg, R.J., Tripathy, A., and Maness, P.F. (2018). Neurocan inhibits semaphorin 3F induced dendritic spine remodeling through NrCAM in cortical neurons. *Front. Cell. Neurosci.* 12, 346. <https://doi.org/10.3389/fncel.2018.00346>.
26. Sullivan, C.S., Gotthard, I., Wyatt, E.V., Bongu, S., Mohan, V., Weinberg, R.J., and Maness, P.F. (2018). Perineuronal net protein neurocan inhibits NCAM/EphA3 repellent signaling in GABAergic interneurons. *Sci. Rep.* 8, 6143. <https://doi.org/10.1038/s41598-018-24272-8>.
27. Li, H., Leung, T.C., Hoffman, S., Balsamo, J., and Lilien, J. (2000). Coordinate regulation of cadherin and integrin function by the chondroitin sulfate proteoglycan neurocan. *J. Cell Biol.* 149, 1275–1288. <https://doi.org/10.1083/jcb.149.6.1275>.
28. Koh, S., Kim, N., Yin, H.H., Harris, I.R., Dejneka, N.S., and Eroglu, C. (2015). Human umbilical tissue-derived cells promote synapse formation and neurite outgrowth via thrombospondin family proteins. *J. Neurosci.* 35, 15649–15665. <https://doi.org/10.1523/JNEUROSCI.1364-15.2015>.
29. Greco, T.M., Seeholzer, S.H., Mak, A., Spruce, L., and Ischiropoulos, H. (2010). Quantitative mass spectrometry-based proteomics reveals the dynamic range of primary mouse astrocyte protein secretion. *J. Proteome Res.* 9, 2764–2774. <https://doi.org/10.1021/pr100134n>.
30. Dowell, J.A., Johnson, J.A., and Li, L. (2009). Identification of astrocyte secreted proteins with a combination of shotgun proteomics and bioinformatics. *J. Proteome Res.* 8, 4135–4143. <https://doi.org/10.1021/pr900248y>.
31. Zhang, Y., Chen, K., Sloan, S.A., Bennett, M.L., Scholze, A.R., O'Keeffe, S., Phatnani, H.P., Guarneri, P., Caneda, C., Ruderisch, N., et al. (2014). An RNA-sequencing transcriptome and splicing database of glia, neurons, and vascular cells of the cerebral cortex. *J. Neurosci.* 34, 11929–11947. <https://doi.org/10.1523/JNEUROSCI.1860-14.2014>.
32. Diniz, L.P., Tortelli, V., Garcia, M.N., Araújo, A.P., Melo, H.M., Silva, G.S., Felice, F.G., Alves-Leon, S.V., Souza, J.M., Romão, L.F., et al. (2014). Astrocyte transforming growth factor beta 1 promotes inhibitory synapse formation via CaM kinase II signaling. *Glia* 62, 1917–1931. <https://doi.org/10.1002/glia.22713>.
33. Wang, L., Liu, W., Li, X., Xiao, X., Li, L., Liu, F., He, Y., Bai, Y., Chang, H., Zhou, D.S., et al. (2018). Further evidence of an association between NCAN rs1064395 and bipolar disorder. *Mol. Neuropsychiatry* 4, 30–34. <https://doi.org/10.1159/000488590>.
34. Wang, D., Zhou, Y., Zhuo, C., Qin, W., Zhu, J., Liu, H., Xu, L., and Yu, C. (2015). Altered functional connectivity of the cingulate subregions in schizophrenia. *Transl. Psychiatry* 5, e575. <https://doi.org/10.1038/tp.2015.69>.
35. Cui, L.B., Liu, J., Wang, L.X., Li, C., Xi, Y.B., Guo, F., Wang, H.N., Zhang, L.C., Liu, W.M., He, H., et al. (2015). Anterior cingulate cortex-related connectivity in first-episode schizophrenia: a spectral dynamic causal modeling study with functional magnetic resonance imaging. *Front. Hum. Neurosci.* 9, 589. <https://doi.org/10.3389/fnhum.2015.00589>.
36. Bouras, C., Kövari, E., Hof, P.R., Riederer, B.M., and Giannakopoulos, P. (2001). Anterior cingulate cortex pathology in schizophrenia and bipolar disorder. *Acta Neuropathol.* 102, 373–379. <https://doi.org/10.1007/s004010100392>.
37. Anticevic, A., Savic, A., Repovs, G., Yang, G., McKay, D.R., Sprooten, E., Knowles, E.E., Krystal, J.H., Pearson, G.D., and Glahn, D.C. (2015). Ventral anterior cingulate connectivity distinguished nonpsychotic bipolar illness from psychotic bipolar disorder and schizophrenia. *Schizophr. Bull.* 41, 133–143. <https://doi.org/10.1093/schbul/sbu051>.
38. Zhou, X.H., Brakebusch, C., Matthies, H., Oohashi, T., Hirsch, E., Moser, M., Krug, M., Seidenbecher, C.I., Boeckers, T.M., Rauch, U., et al. (2001). Neurocan is dispensable for brain development. *Mol. Cell. Biol.* 21, 5970–5978. <https://doi.org/10.1128/MCB.21.17.5970-5978.2001>.
39. Gong, S., Zheng, C., Doughty, M.L., Losos, K., Didkovsky, N., Schambra, U.B., Nowak, N.J., Joyner, A., Leblanc, G., Hatten, M.E., et al. (2003). A gene expression atlas of the central nervous system based on bacterial artificial chromosomes. *Nature* 425, 917–925. <https://doi.org/10.1038/nature02033>.
40. Stogsdill, J.A., Ramirez, J., Liu, D., Kim, Y.H., Baldwin, K.T., Enustun, E., Ejikeme, T., Ji, R.R., and Eroglu, C. (2017). Astrocytic neuroligins control astrocyte morphogenesis and synaptogenesis. *Nature* 551, 192–197. <https://doi.org/10.1038/nature24638>.
41. Zimmermann, D.R., and Dours-Zimmermann, M.T. (2008). Extracellular matrix of the central nervous system: from neglect to challenge. *Histochem. Cell Biol.* 130, 635–653. <https://doi.org/10.1007/s00418-008-0485-9>.
42. Zhang, Y., Sloan, S.A., Clarke, L.E., Caneda, C., Plaza, C.A., Blumenthal, P.D., Vogel, H., Steinberg, G.K., Edwards, M.S., Li, G., et al. (2016). Purification and characterization of progenitor and mature human astrocytes reveals transcriptional and functional differences with mouse. *Neuron* 89, 37–53. <https://doi.org/10.1016/j.neuron.2015.11.013>.
43. Heo, S., Diering, G.H., Na, C.H., Nirujogi, R.S., Bachman, J.L., Pandey, A., and Huganir, R.L. (2018). Identification of long-lived synaptic proteins by proteomic analysis of synaptosome protein turnover. *Proc. Natl. Acad. Sci. USA* 115, E3827–E3836. <https://doi.org/10.1073/pnas.1720956115>.
44. Lee, Y., Messing, A., Su, M., and Brenner, M. (2008). GFAP promoter elements required for region-specific and astrocyte-specific expression. *Glia* 56, 481–493. <https://doi.org/10.1002/glia.20622>.
45. Appella, E., Weber, I.T., and Blasi, F. (1988). Structure and function of epidermal growth factor-like regions in proteins. *FEBS Lett.* 231, 1–4. [https://doi.org/10.1016/0014-5793\(88\)80690-2](https://doi.org/10.1016/0014-5793(88)80690-2).
46. Biermann, B., Ivankova-Susankova, K., Bradaia, A., Abdel Aziz, S., Besseyrias, V., Kapfhammer, J.P., Missler, M., Gassmann, M., and

- Bettler, B. (2010). The SuShi domains of GABAB receptors function as axonal targeting signals. *J. Neurosci.* 30, 1385–1394. <https://doi.org/10.1523/JNEUROSCI.3172-09.2010>.
47. Drickamer, K. (1999). C-type lectin-like domains. *Curr. Opin. Struct. Biol.* 9, 585–590. [https://doi.org/10.1016/S0959-440X\(99\)00009-3](https://doi.org/10.1016/S0959-440X(99)00009-3).
48. Branon, T.C., Bosch, J.A., Sanchez, A.D., Udeshi, N.D., Svinikina, T., Carr, S.A., Feldman, J.L., Perrimon, N., and Ting, A.Y. (2018). Efficient proximity labeling in living cells and organisms with TurboID. *Nat. Biotechnol.* 36, 880–887. <https://doi.org/10.1038/nbt.4201>.
49. Uezu, A., Kanak, D.J., Bradshaw, T.W., Soderblom, E.J., Catavero, C.M., Burette, A.C., Weinberg, R.J., and Soderling, S.H. (2016). Identification of an elaborate complex mediating postsynaptic inhibition. *Science* 353, 1123–1129. <https://doi.org/10.1126/science.aag0821>.
50. Spence, E.F., Dube, S., Uezu, A., Locke, M., Soderblom, E.J., and Soderling, S.H. (2019). In vivo proximity proteomics of nascent synapses reveals a novel regulator of cytoskeleton-mediated synaptic maturation. *Nat. Commun.* 10, 386. <https://doi.org/10.1038/s41467-019-08288-w>.
51. Takano, T., Wallace, J.T., Baldwin, K.T., Purkey, A.M., Uezu, A., Courtland, J.L., Soderblom, E.J., Shimogori, T., Maness, P.F., Eroglu, C., et al. (2020). Chemico-genetic discovery of astrocytic control of inhibition in vivo. *Nature* 588, 296–302. <https://doi.org/10.1038/s41586-020-2926-0>.
52. Courtland, J.L., Bradshaw, T.W.A., Waitt, G., Soderblom, E.J., Ho, T., Rajab, A., Vancini, R., Kim, I.H., and Soderling, S.H. (2021). Genetic disruption of WASHC4 drives endo-lysosomal dysfunction and cognitive-movement impairments in mice and humans. *eLife* 10, e61590. <https://doi.org/10.7554/eLife.61590>.
53. O'Neil, S.D., Rácz, B., Brown, W.E., Gao, Y., Soderblom, E.J., Yasuda, R., and Soderling, S.H. (2021). Action potential-coupled Rho GTPase signaling drives presynaptic plasticity. *eLife* 10, e63756. <https://doi.org/10.7554/eLife.63756>.
54. Cho, K.F., Branon, T.C., Udeshi, N.D., Myers, S.A., Carr, S.A., and Ting, A.Y. (2020). Proximity labeling in mammalian cells with TurboID and split-TurboID. *Nat. Protoc.* 15, 3971–3999. <https://doi.org/10.1038/s41596-020-0399-0>.
55. Song, Y.H., Yoon, J., and Lee, S.H. (2021). The role of neuropeptide somatostatin in the brain and its application in treating neurological disorders. *Exp. Mol. Med.* 53, 328–338. <https://doi.org/10.1038/s12276-021-00580-4>.
56. Sommeijer, J.P., and Levelt, C.N. (2012). Synaptotagmin-2 is a reliable marker for parvalbumin positive inhibitory boutons in the mouse visual cortex. *PLOS One* 7, e35323. <https://doi.org/10.1371/journal.pone.0035323>.
57. Hu, H., Gan, J., and Jonas, P. (2014). Fast-spiking, parvalbumin+GABAergic interneurons: from cellular design to microcircuit function. *Science* 345, 1255263. <https://doi.org/10.1126/science.1255263>.
58. Tremblay, R., Lee, S., and Rudy, B. (2016). GABAergic interneurons in the neocortex: from cellular properties to circuits. *Neuron* 91, 260–292. <https://doi.org/10.1016/j.neuron.2016.06.033>.
59. Llorca, A., and Deogracias, R. (2022). Origin, development, and synaptogenesis of cortical interneurons. *Front. Neurosci.* 16, 929469. <https://doi.org/10.3389/fnins.2022.929469>.
60. Wierenga, C.J., and Wadman, W.J. (1999). Miniature inhibitory postsynaptic currents in CA1 pyramidal neurons after kindling epileptogenesis. *J. Neurophysiol.* 82, 1352–1362. <https://doi.org/10.1152/jn.1999.82.3.1352>.
61. Miles, R., Tóth, K., Gulyás, A.I., Hájos, N., and Freund, T.F. (1996). Differences between somatic and dendritic inhibition in the hippocampus. *Neuron* 16, 815–823. [https://doi.org/10.1016/S0896-6273\(00\)80101-4](https://doi.org/10.1016/S0896-6273(00)80101-4).
62. Risher, W.C., Patel, S., Kim, I.H., Uezu, A., Bhagat, S., Wilton, D.K., Pilaz, L.J., Singh Alvarado, J., Calhan, O.Y., Silver, D.L., et al. (2014). Astrocytes refine cortical connectivity at dendritic spines. *eLife* 3. <https://doi.org/10.7554/eLife.04047>.
63. Eroglu, C., Allen, N.J., Susman, M.W., O'Rourke, N.A., Park, C.Y., Ozkan, E., Chakraborty, C., Mulinyawe, S.B., Annis, D.S., Huberman, A.D., et al. (2009). Gabapentin receptor alpha2delta-1 is a neuronal thrombospondin receptor responsible for excitatory CNS synaptogenesis. *Cell* 139, 380–392. <https://doi.org/10.1016/j.cell.2009.09.025>.
64. Mauch, D.H., Nägler, K., Schumacher, S., Görz, C., Müller, E.C., Otto, A., and Pfrieger, F.W. (2001). CNS synaptogenesis promoted by glia-derived cholesterol. *Science* 294, 1354–1357. <https://doi.org/10.1126/science.294.5545.1354>.
65. Baldwin, K.T., Tan, C.X., Strader, S.T., Jiang, C., Savage, J.T., Elorza-Vidal, X., Contreras, X., Rülicke, T., Hippenmeyer, S., Estévez, R., et al. (2021). HepaCAM controls astrocyte self-organization and coupling. *Neuron* 109, 2427–2442.e10. <https://doi.org/10.1016/j.neuron.2021.05.025>.
66. Schuman, B., Machold, R.P., Hashikawa, Y., Fuzik, J., Fishell, G.J., and Rudy, B. (2019). Four unique interneuron populations reside in neocortical Layer 1. *J. Neurosci.* 39, 125–139. <https://doi.org/10.1523/JNEUROSCI.1613-18.2018>.
67. Tuncdemir, S.N., Wamsley, B., Stam, F.J., Osakada, F., Goulding, M., Callaway, E.M., Rudy, B., and Fishell, G. (2016). Early somatostatin interneuron connectivity mediates the maturation of deep layer cortical circuits. *Neuron* 89, 521–535. <https://doi.org/10.1016/j.neuron.2015.11.020>.
68. Su, J., Basso, D., Iyer, S., Su, K., Wei, J., and Fox, M.A. (2020). Paracrine role for somatostatin interneurons in the assembly of perisomatic inhibitory synapses. *J. Neurosci.* 40, 7421–7435. <https://doi.org/10.1523/JNEUROSCI.0613-20.2020>.
69. Cossart, R. (2011). The maturation of cortical interneuron diversity: how multiple developmental journeys shape the emergence of proper network function. *Curr. Opin. Neurobiol.* 21, 160–168. <https://doi.org/10.1016/j.conb.2010.10.003>.
70. Niquille, M., Limoni, G., Markopoulos, F., Cadilhac, C., Prados, J., Holtmaat, A., and Dayer, A. (2018). Neurogliaform cortical interneurons derive from cells in the preoptic area. *eLife* 7, e32017. <https://doi.org/10.7554/eLife.32017>.
71. Liddelow, S.A., Guttenplan, K.A., Clarke, L.E., Bennett, F.C., Bohlen, C.J., Schirmer, L., Bennett, M.L., Münch, A.E., Chung, W.S., Peterson, T.C., et al. (2017). Neurotoxic reactive astrocytes are induced by activated microglia. *Nature* 541, 481–487. <https://doi.org/10.1038/nature21029>.
72. Mizuno, H., Warita, H., Aoki, M., and Itoyama, Y. (2008). Accumulation of chondroitin sulfate proteoglycans in the microenvironment of spinal motor neurons in amyotrophic lateral sclerosis transgenic rats. *J. Neurosci. Res.* 86, 2512–2523. <https://doi.org/10.1002/jnr.21702>.
73. Hußler, W., Höhn, L., Stoltz, C., Vielhaber, S., Garz, C., Schmitt, F.C., Gundelfinger, E.D., Schreiber, S., and Seidenbecher, C.I. (2022). Brevican and neurocan cleavage products in the cerebrospinal fluid - differential occurrence in ALS, epilepsy and small vessel disease. *Front. Cell. Neurosci.* 16, 838432. <https://doi.org/10.3389/fncel.2022.838432>.
74. Galbiati, M., Crippa, V., Rusmini, P., Cristofani, R., Messi, E., Piccolella, M., Tedesco, B., Ferrari, V., Casarotto, E., Chierichetti, M., et al. (2020). Multiple roles of transforming growth factor beta in amyotrophic lateral sclerosis. *Int. J. Mol. Sci.* 21. <https://doi.org/10.3390/ijms21124291>.
75. Li, W. (2022). Excitation and inhibition imbalance in Rett syndrome. *Front. Neurosci.* 16, 825063. <https://doi.org/10.3389/fnins.2022.825063>.
76. Boggio, E.M., Lonetti, G., Pizzorusso, T., and Giustetto, M. (2010). Synaptic determinants of Rett syndrome. *Front. Synaptic Neurosci.* 2, 28. <https://doi.org/10.3389/fnsyn.2010.00028>.
77. Caldwell, A.L.M., Sancho, L., Deng, J., Bosworth, A., Miglietta, A., Diedrich, J.K., Shokhirev, M.N., and Allen, N.J. (2022). Aberrant astrocyte protein secretion contributes to altered neuronal development in multiple models of neurodevelopmental disorders. *Nat. Neurosci.* 25, 1163–1178. <https://doi.org/10.1038/s41593-022-01150-1>.
78. Morris, H.M., Hashimoto, T., and Lewis, D.A. (2008). Alterations in somatostatin mRNA expression in the dorsolateral prefrontal cortex of subjects with schizophrenia or schizoaffective disorder. *Cereb. Cortex* 18, 1575–1587. <https://doi.org/10.1093/cercor/bhm186>.

79. Guillozet-Bongaarts, A.L., Hyde, T.M., Dalley, R.A., Hawrylycz, M.J., Henry, A., Hof, P.R., Hohmann, J., Jones, A.R., Kuan, C.L., Royall, J., et al. (2014). Altered gene expression in the dorsolateral prefrontal cortex of individuals with schizophrenia. *Mol. Psychiatry* 19, 478–485. <https://doi.org/10.1038/mp.2013.30>.
80. Lin, L.C., and Sibille, E. (2013). Reduced brain somatostatin in mood disorders: a common pathophysiological substrate and drug target? *Front. Pharmacol.* 4, 110. <https://doi.org/10.3389/fphar.2013.00110>.
81. Savage, J.T., Ramirez, J., Risher, W.C., Irala, D., and Eroglu, C. (2023). SynBot: an open-source image analysis software for automated quantification of synapses. *bioRxiv*. <https://doi.org/10.1101/2023.06.26.546578>.
82. Modzelewski, A.J., Chen, S., Willis, B.J., Lloyd, K.C.K., Wood, J.A., and He, L. (2018). Efficient mouse genome engineering by CRISPR-EZ technology. *Nat. Protoc.* 13, 1253–1274. <https://doi.org/10.1038/nprot.2018.012>.
83. Falk, T., Mai, D., Bensch, R., Çiçek, Ö., Abdulkadir, A., Marrakchi, Y., Böhm, A., Deubner, J., Jäckel, Z., Seiwald, K., et al. (2019). U-net: deep learning for cell counting, detection, and morphometry. *Nat. Methods* 16, 67–70. <https://doi.org/10.1038/s41592-018-0261-2>.
84. Risher, W.C., Kim, N., Koh, S., Choi, J.E., Mitev, P., Spence, E.F., Pilaz, L.J., Wang, D., Feng, G., Silver, D.L., et al. (2018). Thrombospondin receptor $\alpha 2\delta-1$ promotes synaptogenesis and spinogenesis via postsynaptic Rac1. *J. Cell Biol.* 217, 3747–3765. <https://doi.org/10.1083/jcb.201802057>.

STAR★METHODS

KEY RESOURCES TABLE

REAGENT or RESOURCE	SOURCE	IDENTIFIER
Antibodies		
Actin	Sigma-Aldrich	Cat# A5441; RRID: AB_476744
Bassoon	Enzo/Assay Designs	Cat# ADI-VAM-PS003F; RRID: AB_11181058
Ctip2	Abcam	Cat# Ab18465; RRID: AB_2064130
GAD-67	Millipore	MAB5406; RRID:AB_2278725
Gephyrin	Synaptic Systems	Cat# 147 002; RRID:AB_2619838
Gephyrin	Synaptic Systems	Cat# 147 011; RRID:AB_887717
GFAP	Sigma	Cat# G3893; RRID:AB_477010
GFP	Aves labs	GFP-1020; RRID:AB_10000240
HA	Roche	11867423001; RRID:AB_390918
HA	Aves Labs	Cat# ET-HA100; RRID:AB_2313511
Homer1	Synaptic systems	Cat# 160 002; RRID: AB_2120990
Homer1	Synaptic systems	Cat#160011; RRID: AB_2120992
L1 (ASCS4)	DSHB	Cat# ascs4; RRID:AB_528349
LHX2	Millipore	Cat# ABE1402; RRID: AB_2722523
MAP2	Abcam	Cat# ab32454; RRID:AB_1001650
NCAN C-Terminal	Invitrogen	Cat# PA5-79718; RRID: AB_2746833
NCAN N-Terminal	R&D Systems	Cat#AF5800; RRID: AB_2149717
NeuN (A60)	Millipore	Cat# MAB377; RRID:AB_2298772
NeuN	Millipore	Cat# ABN78; RRID:AB_10807945
Olig2 (211F.1)	Millipore	Cat# MABN50; RRID:AB_10807410
Parvalbumin	Abcam	Cat# ab11427; RRID:AB_298032
PSD-95	Life Technologies	Cat# 51-6900; RRID:AB_87705
Somatostatin	Bma Biomedicals Ag	Cat# T-4103; RRID:AB_518614
Somatostatin	Millipore	Cat# MAB354; RRID: AB_2255365
Sox9	Millipore	Cat# AB5535; RRID:AB_2239761
Synaptotagmin-2	Synaptic Systems	Cat# 105 225; RRID: AB_2744654
Synaptotagmin-2	Synaptic Systems	Cat# 105 223; RRID: AB_10894084
TBR1	Abcam	Cat#31940; RRID: AB_2200219
VGAT	Synaptic Systems	Cat# 131 004; RRID:AB_887873
VGluT1	Millipore	Cat# AB5905; RRID:AB_2301751
WFA	Vector Laboratories	Cat# B-1355
Bacterial and virus strains		
One Shot STBL3	Thermo Fisher	Cat# C737303
AAV PhP.eB	This paper	N/A
Chemicals, peptides, and recombinant proteins		
AraC	Sigma	Cat# C1768
B27	GIBCO	Cat# 17504044
B27 Plus	GIBCO	Cat# A3582801
BDNF	PeproTech	Cat# 450-02
Carboxypeptidase E	R&D	Cat# 3587-ZN
CNTF	PeproTech	Cat# 450-13
Clusterin	R&D	Cat# 2937-HS

(Continued on next page)

Continued

REAGENT or RESOURCE	SOURCE	IDENTIFIER
DMEM	GIBCO	Cat# 11960
DPBS	GIBCO	Cat# 14287
Dystroglycan	R&D	Cat# 6868-DG
Fetal Bovine Serum	Thermo Fisher	Cat# 10-437-028
Forskolin	Sigma	Cat# F6886
Glycerol	Acros Organics	Cat# AC158920010
L-glutamine	GIBCO	Cat# 25030-081
Hydrocortisone	Sigma	Cat# H0888-5G
Insulin	Sigma	Cat# I1882
Neurobasal	GIBCO	Cat# 21103049
Neurobasal Plus	GIBCO	Cat# A3582901
Neurobasal minus Phenol Red	GIBCO	Cat# 12348017
Neurocan Full-Length	This paper	N/A
Neurocan ELS	This paper	N/A
Neurocan IL	This paper	N/A
Odyssey Blocking Buffer	LI-COR Biosciences	Cat# 927-40000
Opti-MEM	Thermo Fisher	Cat# 11058021
Paraformaldehyde	Electron microscopy Sciences	Cat# 19210
Pen/Strep	GIBCO	Cat# 15140
PhosSTOP™	Roche	Cat# 4906845001
Poly-D-lysine	Sigma	Cat# P6407
Protease Inhibitor Cocktail	Roche	Cat# 4693132001
RIPA Buffer	Sigma	Cat# R0278
Sodium Pyruvate	GIBCO	Cat# 11360-070
DyLight 594 Streptavidin	Vector Laboratories	Cat# SA-5594
TGFβ1	R&D	Cat# 7666-MB
Tissue-Tek® O.C.T. Compound	Sakura® Finetek	Cat# 4583
Triton X-100	Roche	Cat# 11332481001
Critical commercial assays		
Endo-free Maxi Prep Kit	QIAGEN	Cat# 12362
Deposited data		
TurboID Mass Spectrometry Data	This paper	MassIVE: MSV000091630
Experimental models: Cell lines		
HEK293T	ATCC	CRL-11268
Rat Primary Cortical Neurons	This paper	N/A
Rat Primary Cortical Astrocytes	This paper	N/A
Mouse Primary Cortical Astrocytes	This paper	N/A
Experimental models: Organisms/strains		
Mouse: Aldh1L1-EGFP	MMRRC	RRID:MMRRC_011015-UCD
Mouse: CD1	Charles River	RRID:IMSR_CRL:022
Mouse: Neurocan KO	This paper	N/A
Mouse: Neurocan ΔELS	This paper	N/A
Rat: Sprague-Dawley	Charles River	001
Oligonucleotides		
See Table S5 – Materials and methods		N/A
Oligonucleotides		

(Continued on next page)

Continued

REAGENT or RESOURCE	SOURCE	IDENTIFIER
Recombinant DNA		
pZac2.1-GfaABC1D -IgK- TurboID- NCAN IL-HA	This paper	N/A
pZac2.1-GfaABC1D -IgK- TurboID- NCAN ELS-HA	This paper	N/A
pZac2.1-GfaABC1D -IgK-TurboID-HA	This paper	N/A
pZac2.1-GfaABC1D -TurboID-HA	Takano et al. ⁵¹	N/A
pZac2.1-GfaABC1D -IgK-NCAN ELS-HA	This paper	N/A
pAPtag5-IgK-NCAN-Full Length	This paper	N/A
pAPtag5-IgK-NCAN ELS	This paper	N/A
pAPtag5-IgK- NCAN IL	This paper	N/A
pmaxGFP	Lonza	N/A
Software and algorithms		
GraphPad Prism 8	GraphPAD	https://www.graphpad.com/scientific-software/prism/
ImageJ	NIH	https://imagej.nih.gov/ij/
Puncta Analyzer	Savage et al. ⁸¹	https://github.com/Eroglu-Lab/Syn_Bot
Image Studio	LICOR	https://www.licor.com
Other		
Digital Restoration and Image Segmentation	Baldwin et al. ⁶⁵	https://github.com/ErogluLab/CellCounts
Area colocalization for smRNA FISH Macro	This paper	https://github.com/Eroglu-Lab/Irala_2024_image_analysis[https://doi.org/10.5281/zenodo.10779514]
Puncta Analyzer around Cell Body Macro	This paper	https://github.com/Eroglu-Lab/Irala_2024_image_analysis[https://doi.org/10.5281/zenodo.10779514]

RESOURCE AVAILABILITY

Lead contact

Further information and requests for resources and reagents should be directed to and will be fulfilled by the lead contact, Dolores Irala (dolores.irala@duke.edu).

Materials availability

The reagents generated in this study are available without restriction.

Data and code availability

The data generated during this study are available from the lead contact upon request. The proteomic data is uploaded in the repository Massive (massive.ucsd.edu), accession number: MSV000091630.

All original code has been deposited at Zenodo and is publicly available as of the date of publication. DOIs are listed in the key resources table.

Any additional information required to reanalyze the data reported in this work paper is available from the Lead Contact upon request.

EXPERIMENTAL MODEL AND SUBJECT DETAILS

Animals

All rodents in this study were used in accordance with the Institutional Animal Care and Use Committee (IACUC) and the Duke Division of Laboratory Animal Resources (DLAR) oversight (IACUC Protocol Numbers A147-17-06 and A117-20-05). All mice were housed under typical day/night conditions of 12-hour cycles. Aldh1L1-EGFP (RRID:MMRRC_011015-UCD) mice were obtained through MMRRC. WT CD1 mice used for immunofluorescence, western blot, and TurboID experiments were purchased through Charles River Laboratories (RRID:IMSR_CRL:022). Neurocan knockout mice and neurocan ΔELS mutant mice were generated in

collaboration with the Duke Transgenic Mouse Facility using CRISPR-EZ protocol from Modzelewski et al.⁸² Briefly, single guide RNA (sgRNA) was designed and then generated by in-vitro transcription of a short DNA template. After donor superovulation, pronuclear-stage embryos were collected, cultured, and electroporated with the sgRNA and Cas9 Ribonucloprotein (IDT, Alt-R Cas9 v3 Cat#1081059). Viable embryos were cultured and genotyped *ex vivo* to test the sgRNA efficiency. Successful embryos were oviduct transferred to pseudopregnant CD1 females. After birth, funders were screened by PCR with genomic DNA. PCR products were subcloned into pL253 at the NotI-Spel restriction sites. From each funder, independent subclones were sequenced to identify the targeted mutation. P1, P7, P10, P15, P21 and P30 mice were used for experiments or as specified in the text and figure legends. Littermate pairs of the same sex were used for all the experiments and were randomly assigned to experimental groups based on genotype. Mice of both sexes were included in the analysis of each experiment, and no influence or association of sex on the experimental outcomes was observed for any of the results.

METHOD DETAILS

Primary cultures

Cortical neuron isolation and culture

Postnatal glia-free rat cortical neuronal cultures were prepared from male P1 rat pups (Sprague Dawley, Charles River Laboratories, SD-001). Cerebral cortices were micro-dissected and enzymatically dissociated with papain (~7.5 units/mL) at 33°C for 45 minutes. After incubation, the cortices were mechanically dissociated in low and high ovomucoid solutions to obtain a single-cell suspension. Next the cells were resuspended in panning buffer (DPBS (GIBCO 14287) supplemented with BSA and insulin) and passed through a 20 µm mesh filter (Elko Filtering 03-20/14) to remove any debris. The filtered cells were incubated on negative panning dishes coated with Bandeiraea simplicifolia Lectin 1 (x2), followed by goat anti-mouse IgG+IgM (H+L) (Jackson ImmunoResearch 115-005-044), and goat anti-rat IgG+IgM (H+L) (Jackson ImmunoResearch 112-005-044) coated plates. Finally, the cells were incubated for 45 minutes on positive panning dishes coated with mouse anti-rat L1 (ASCS4, Developmental Studies Hybridoma Bank, Univ. Iowa) to bind only cortical neurons. After incubation, the positive plates were washed with panning buffer and the remaining adherent cells were collected by forceful pipetting with a P1000 pipette. Isolated neurons were pelleted (11 min at 200 g) and resuspended in serum-free neuron growth media (NGM; Neurobasal, B27 supplement, 2 mM L-glutamine, 100 U/mL Pen/Strep, 1 mM sodium pyruvate, 4.2 µg/mL forskolin, 50 ng/mL BDNF, and 10 ng/mL CNTF). 70,000 neurons were plated onto 12 mm glass coverslips coated with 10 µg/mL poly-D-lysine (PDL, Sigma P6407) and 2 µg/mL laminin. The neurons were incubated at 37°C in 10% CO₂. On day *in-vitro* (DIV) 2, half of the media was replaced with NGM Plus (Neurobasal Plus, B27 Plus, 100 U/mL Pen/Strep, 1 mM sodium pyruvate, 4.2 µg/mL forskolin, 50 ng/mL BDNF, and 10 ng/mL CNTF) supplemented with AraC (4 µM). On DIV 3, all of the media was replaced with NGM Plus to remove any traces of AraC. At DIV 6 the neurons were fed with NGM Plus. On DIV 8 and DIV 11 the neurons were fed with NGM Plus with ACM or recombinant proteins as indicated on each experiment.

Cortical astrocyte isolation and culture

Rat and mouse cortical astrocytes were prepared as described previously.⁴⁰ Briefly, P1 rat or mouse cortices from both sexes were micro-dissected, enzymatically dissociated with papain, mechanically dissociated in low and high ovomucoid solutions, and resuspended in astrocyte growth media (AGM: DMEM (GIBCO 11960), 10% FBS, 10 µM hydrocortisone, 100 U/mL Pen/Strep, 2 mM L-glutamine, 5 µg/mL insulin, 1 mM Na pyruvate, 5 µg/mL N-acetyl-L-cysteine). Between 20 million cells were seeded on 75 mm² flasks (non-ventilated cap) coated with poly-D-lysine and incubated at 37°C in 10% CO₂. On DIV 3, non-astrocyte cells were removed by forcefully shaking the flasks until only an adherent monolayer of astrocytes remained. AraC was added to the media from DIV 5 to DIV 7 to eliminate contaminating fibroblasts. On DIV 7, astrocytes were trypsinized (0.05% trypsin-EDTA) and plated into 10cm dishes with AGM. For astrocyte-conditioned media production, on DIV 8 the media was replaced with minimal media (Neurobasal medium, minus phenol red, 100 U/mL Pen/Strep, 2 mM L-glutamine, 1 mM Na pyruvate), and the astrocytes were incubated for 4 days. At DIV 12 the astrocyte-conditioned media was collected, filtered, and concentrated using Vivaspin 20, 5kDa MWCO. For astrocyte transfection, at DIV 8 the astrocytes were transfected with the expression plasmids using Lipofectamine LTX with Plus Reagent (Thermo Scientific) per the manufacturer's protocol.

Cell lines

HEK293T cells

HEK293 cells were used to produce adeno-associated virus and recombinant proteins. Cells were cultured in DMEM supplemented with 10% fetal bovine serum, 100 U/mL Pen/Strep, 2 mM L-glutamine, and 1 mM sodium pyruvate. The cells were incubated at 37°C in 5% CO₂ and passaged every 2–3 days.

shRNA and cDNA plasmids

NCAN expression constructs—Recombinant proteins

To produce His-tag NCAN Full-length, NCAN IL-domain, and NCAN ELS DNA plasmids gene block fragments that codify for those sequences were produced in the Duke Transgenic Mouse Facility. Each gene block fragment was inserted into a vector backbone

pAPtag5 using Xba1 and Nhe1 enzyme sites. The secretion signal peptide IgK leader sequence was inserted in the N-terminal of each gene block to promote the equal secretion of the resulting proteins. A 6X His-tag was added to the C-terminal of each fragment for detection. All constructs were confirmed by DNA sequencing.

NCAN expression constructs—Astrocyte-specific rescue

To generate the pZac2.1-GfaABC1D-IgK-NCAN ELS-HA construct, the NCAN C-terminal fragment was initially obtained by performing a restriction digestion on pAPtag5-IgK-NCAN ELS using Nhe1 and Xba1 enzymes. Subsequently, the eluted NCAN C-terminal fragment underwent further cloning into the pZac2.1 vector backbone, resulting in the construction of pZac2.1-GfaABC1D-IgK-NCAN ELS-HA. To validate the integrity of the construct, Sanger sequencing was conducted using specific primers designed for the confirmation of both the orientation of directional cloning and the presence of the intended inserts.

TurboID expression constructs

Cytosolic pZac2.1_GFABC1D-Turbo-BirA-HA construct was a gift from Soderling Lab.⁵¹ IgK-TurboID, IgK-TurboID-NCAN IL-HA and, IgK-TurboID-NCAN ELS-HA were cloned into pZac2.1_GFABC1D-Turbo-BirA-HA construct from Takano et al.⁵¹. To generate these constructs gene block fragments that codify for those sequences were produced in the Duke Transgenic Mouse Facility and cloned into the backbone using EcoRI-HF Restriction Enzyme (NEB) and In-Fusion HD Cloning Kit (TaKaRa) following the manufacturer's protocol.

His-tagged protein purification

For NCAN Full-length, NCAN IL-domain, and NCAN ELS His-tag protein purification, DNA plasmid of each condition was transfected to 10cm dishes of HEK cells. Two days after transfection the HEK cells were washed with PBS and conditioned with DMEM minimal media (DMEM medium minus phenol red, 100 U/mL Pen/Strep, 2 mM L-glutamine, 1 mM Na pyruvate) for four days. Next, the conditioned medium was collected and concentrated using Vivaspin 20, 5kDa MWCO. After concentration, the medium was mixed with Ni-NTA resin (Qiagen) and incubated overnight at 4°C while gently nutating. Next the Ni-NTA agarose beads were washed with DPBS then collected in a Poly-Prep chromatography column (Thermo Fisher). NCAN Full-length, NCAN IL-domain, and NCAN ELS His-tag peptide fragments were eluted by competition with 250 mM imidazole in DPBS. The final concentration was measured using BCA protein assay kit (Thermo) per manufacturer's protocol.

Immunocytochemistry

In vitro

Neuronal or astrocyte cultures on glass coverslips were fixed on DIV 12 with warm 4% PFA for 7 minutes and then washed 3 times with PBS to remove any excess of PFA. The neurons were blocked in a blocking buffer containing 50% normal goat serum (NGS) and 0.2% Triton X-100 for 30 minutes. After removal of the blocking buffer, the cells were incubated overnight at 4°C in primary antibodies diluted in blocking buffer containing 10% NGS. After primary antibody incubation, the neuronal cultures were washed with PBS three times and incubated in Alexa Fluor conjugated secondary antibodies and DAPI (Vector Labs) diluted in a blocking buffer containing 10% NGS for 1 hour at room temperature. Finally, the cells were washed again in PBS three times. The coverslips were mounted onto glass slides (VWR Scientific) with a homemade mounting media (90% glycerol, 20 mM Tris pH 8.0, 0.5% n-propyl gallate) and sealed with nail polish. Imaging of single optical sections of synaptic markers or astrocyte markers was acquired using an Olympus FV 3000 microscope with a 60x objective and 2x optical zoom. The imaging was always blind to the experimental condition and individual neurons or astrocytes were selected using DAPI. For synaptic analysis, inhibitory and excitatory synapse numbers were obtained using the ImageJ software SynBot³¹ (https://github.com/Eroglu-Lab/Syn_Bot). The same circular area of interest around each neuron was analyzed. In all cases, a minimum of 3 independent experiments were performed as indicated in the figure legend for each experiment. 20 cells were imaged per condition per experiment.

Neuronal morphology analysis

Postnatal glia-free rat cortical neuronal cultures were prepared from male P1 rat pups as described before in material and methods section. Neurons were transfected with GFP plasmid at DIV5 after AraC treatment. Astrocyte-conditioned medium or NCAN ELS recombinant protein was added to the cultures at DIV8 and DIV11. The neuronal cultures were fixed at DIV13 with warm 4% PFA for 7 minutes and then washed 3 times with PBS to remove any excess of PFA. For the staining, the neurons were blocked in a blocking buffer containing 50% normal goat serum (NGS) and 0.2% Triton X-100 for 30 minutes. Next, the cells were incubated overnight at 4°C in primary antibodies (anti- GFP, MAP2, and VGlut1) diluted in blocking buffer containing 10% NGS. After primary antibody incubation, the neuronal cultures were washed with PBS and incubated in blocking buffer containing Alexa Fluor conjugated secondary antibodies and DAPI (Vector Labs) for 1 hour at room temperature. Finally, the cells were washed again in PBS three times. The coverslips were mounted onto glass slides (VWR Scientific) with a homemade mounting media (90% glycerol, 20 mM Tris pH 8.0, 0.5% n-propyl gallate) and sealed with nail polish. Images were obtained using a Keyence BZ-X800 microscope. Each image was taken using a 20x magnification objective. Dendrite length and branching points were manually counted using Fiji.

In vivo

Mice were anesthetized with 200 mg/kg tribromoethanol (Avertin) and perfused with TBS/heparin and 4% PFA. Following perfusion, the brains were collected and fixed overnight in 4% PFA solution. Next, the brains were washed with TBS to remove any residual PFA and cryoprotected in 30% sucrose. The brains were frozen and stored at -80 in a solution containing 2 parts 30% sucrose and 1-part O.C.T. (TissueTek). The day before immunostaining the brains were sectioned using a cryostat to obtain floating coronal tissue sections of 40 µm thickness and stored in a 1:1 mixture of TBS/glycerol at -20°C. Sections were washed in 1x TBS containing 0.2%

Triton X-100 (TBST) for 10 minutes 3 times and then blocked in 10% NGS diluted in TBST. Following blocking the sections were incubated in primary antibody for 48hs at 4°C with shaking. After primary incubation, sections were washed in TBST for 10 minutes 3 times and incubated in Alexa Fluor conjugated secondary antibodies diluted 1:200 (Life Technologies) with DAPI (1:50,000) for 2 hours at room temperature shaking. After this incubation, the sections were washed with TBST for 10 minutes 3 times and mounted onto glass slides using a homemade mounting media (90% glycerol, 20 mM Tris pH 8.0, 0.5% n-propyl gallate) and sealed with nail polish. All the images were acquired on confocal Olympus FV 3000 microscope or confocal Leica Stellaris 8 microscope. For STED microscopy, the samples were prepared as described above with changes in primary and secondary antibodies. Primary antibodies were used more concentrated depending on the antibody, and secondary antibody concentrations were used at 1:100. STED-optimized secondary fluorophores were used: Oregon Green 488, Alexa Fluor 488, Alexa Fluor 594 and abberior STAR RED). STED images were acquired on a Leica SP8 STED microscope using a white light excitation laser, 775 depletion laser (red and far red channels), and 560 depletion laser (green channel). Deconvolution of STED images was performed using Huygens Professional software. The researcher acquiring the images was blinded to the experimental group.

Cell counting imaging and analysis

Cell counting was performed as described in Baldwin et al.⁶⁵ Briefly, tile scan images containing the anterior cingulated cortex from P30 Ncan WT, Ncan KO or Ncan ΔELS mutant mice were rapidly acquired on an Olympus FV 3000 using the resonant scanner and 20x objective. For labeled nuclei marked with NeuN, Sox9 or Olig2 nuclear markers were identified using a machine-learning-based method for imaged segmentation (U-Net).⁸³ Full source code for this method is available here: <https://github.com/ErogluLab/CellCounts>. Co-localization of two nuclear markers was determined in ImageJ. 3 sections per brain from 3 sex-matched littermate groups were analyzed.

For GAD67+ interneuron counting in the ACC, tile scan images from P30 Ncan WT, Ncan KO or Ncan ΔELS mutant mice were acquired on the Olympus FV 3000 using the resonant scanner and 20x objective. The number of cells labeled GAD67 was quantified by hand using the cell counter tool in ImageJ. 3 sections per brain from 3 sex-matched littermate groups were analyzed.

Synapse imaging and analysis

Synapse staining, imaging, and acquisition were performed as previously described.^{65,84} Briefly, 40 μm thick coronal sections from NCAN WT, NCAN KO or NCAN ΔELS mutant mice containing the anterior cingulate cortex were used. To label inhibitory synapses VGAT and gephyrin synaptic markers were used and for excitatory synapses VGlUT1 and PSD95 markers we used. To label somatostatin+ synapses we used SST and gephyrin synaptic markers, and for perisomatic parvalbumin synapses Syt2, NeuN and gephyrin antibody were used. Images were obtained using a Confocal Olympus FV 3000 or confocal Leica Stellaris 8 inverted microscopes. For the Confocal Olympus FV 3000, each image was taken using a 60x magnification objective with 1.64x optical zoom. Each z-stack image contains 15 optical sections spaced 0.34 μm apart. For confocal Leica Stellaris 8 microscope, each image was taken using a 93x magnification objective. Each z-stack image contains 15 optical sections spaced 0.34 μm apart. Synapses were identified by the colocalization of pre and postsynaptic puncta. Excitatory, inhibitory and SST+ synapse numbers were obtained using the ImageJ software SynBot⁸¹ (https://github.com/Eroglu-Lab/Syn_Bot). 3 sections per brain from 6 sex-matched littermate groups were analyzed. In the ACC, L1, L2-3 and L5 at P30. To analyze perisomatic PV+ synapses, we used a custom made plugin that expand NeuN signal and quantify the number of colocalization of Syt2 with gephyrin inside of the NeuN mask, available at https://github.com/Eroglu-Lab/Irala_2024_image_analysis. In this paper we used an NeuN expansion of 10 pixels.

STED analysis

Perineuronal net analysis and synaptic colocalization in Ncan WT, Ncan KO or Ncan ΔELS mutant mice was acquired with 93x objective using 5x zoom at a resolution of 2048 × 2048 pixels, for 5 optical sections spaced 0.15 μm apart. Next, the images were deconvolved using Huygens Professional software and maximum projection images representing 0.6 μm in the z-direction were generated for analysis. NCAN C-terminal puncta localization at synapses was quantified by hand using the cell counter tool in ImageJ. 3 sections per brain from 3 sex-matched WT CD1 littermate groups were analyzed as described in the figure legend.

Multiplexed immunofluorescence and RNA-FISH for simultaneous detection of protein and RNA targets

Custom-made probes for Ncan were acquired from Molecular Instruments. Buffers were purchased from Molecular Instruments. Protocol used from manufactured. Briefly, five 20 μm sections of prefrontal cortex from P7, P14, P21, and P30 Aldh1L1-EGFP brains were directly mounted onto glass slides. All sections were kept at -80°C until use. First, sections were thawed for 5 minutes at room temperature, washed three times with 1X PBS containing 0.1% Tween20 (PBST), blocked in 200 μl of antibody buffer at room temperature for 1 h, and incubated in a wet chamber with anti-GFP (1:1,000) primary antibody overnight at 4°C. After overnight incubation, the sections were washed with PBST, followed by 1 h incubation at room temperature with 100 μl initiator-labeled secondary antibody diluted in antibody buffer. Next, the sections were washed in PBST, postfixed in 200 μl of 4% PFA for 10 min, and immersed in 5× sodium chloride sodium citrate containing 0.1% Tween20 (5× SSCT) for 5 min to prime the sections for RNA probe hybridization. 100 μl of 16 nM of Ncan probe solution was applied to the sections for incubation overnight in a 37°C humidified chamber. The following day, the sections were incubated in a mixture of probe wash buffer and 5× SSCT at 37°C to remove the probe excess. Each incubation had an increasing concentration of 5× SSCT, ending with a final incubation of 100% 5× SSCT. Next, 200 μl of amplification buffer was added to the sections for 30 min at room temperature. Snap-cooled hairpins specific to the initiator-labeled secondary antibody and Ncan probe were mixed with the amplification buffers resulting in a 60 mM hairpin solution. The sections were

incubated with 100 µl of this mixture at room temperature overnight. Finally, the sections were immersed in 5× SSCT for a total of 45 min to remove excess hairpins, dried, and mounted with mounting media.

The resulting sections were imaged within 2 days at high magnification (60× objective with 2X optical zoom) and resolution (1 µm step size, 6 µm z-stack) on an Olympus FV 3000 microscope. In total, 108 images were taken for the entire dataset (images of L1, L2-3, and L5 of each section, three sections per animal, three animals per time point for P7, P14, P21 and P30). The images were then processed using a Fiji custom pipeline that includes thresholding of *Ncan* signal and colocalization area with GFP positive astrocyte area. The software used for this analysis can be found here https://github.com/Eroglu-Lab/Irala_2024_image_analysis.

Protein extraction and western blotting

Protein was extracted from mouse or rat astrocyte cultures using RIPA buffer with protease inhibitors. Cell lysates were collected, incubated on ice for 10 minutes, and centrifuged at 4°C at high speed for 10 minutes to pellet non-solubilized material. The supernatant was collected and stored at -80°C.

To collect protein from brain cortices, mice P7 or younger were euthanized via rapid decapitation, and mice older than P7 were euthanized using chamber CO₂ administration. Cortices were micro-dissected and mechanically dissociated using RIPA buffer with protease inhibitor in a dounce homogenizer with teflon pestle. After getting the homogenate, the samples were collected and incubated at 4°C in a rotor for 15 minutes. Next, the samples were centrifuged at high speed for 10 minutes to pellet non-solubilized material. The supernatant was collected and stored at -80°C.

To remove the glycosaminoglycan chains the samples were treated with chondroitinase ABC (1:20 of 20 U/ml stock, Sigma-Aldrich C3667) at 37°C for 90 min. Pierce BSA Protein Assay Kit (Thermo Fisher) was used to determine protein concentration. The lysates were mixed with 2x Laemmli Sample Buffer (BioRad) containing 5% β-ME and incubated at 95°C for 5 minutes to denature proteins. Samples were loaded into 4%-15% gradient pre-cast gels (Bio-Rad) and run at 100 V for 1 hour. Proteins were transferred at 100 V to PVDF membrane (Millipore) for 2 hours, blocked BSA 3% in TBS 0.001% Tween-20 and incubated rocking in primary antibody overnight at 4°C. After overnight incubation, the membranes were washed rocking with TBS 0.001% Tween-20 5 times of 10 minutes, incubated in LI-COR secondary antibodies for one hour, washed rocking with TBS 0.001% Tween-20 5 times of 10 minutes, and imaged on an Odyssey infrared Imaging system using Image Studio software. Protein expression was quantified using Image Studio Lite software.

Adeno-associated virus (AAV) production and administration

Purified AAV was produced in house and in collaboration with the Duke University Viral Vector Core facility. Briefly, HEK293T cells were co-transfected with 3 plasmids: pAd-DELTA F6 (plasmid No. 112867; Addgene), serotype plasmid AAV PHP.eB, and AAV plasmid (pZac2.1-gfaABC1D-TurboID constructs). After transfection, cells were lysed and the replicated viral vectors were collected, purified and stored at -80°C. The viral titer for each vector was calculated by real-time PCR.

In vivo rescue experiment

AAV viruses were administrated intracortical in P1 NCAN WT and KO mouse pups. Pups were anesthetized by hypothermia and 1µl of each concentrated AAV vector was injected bilaterally into the cortex using a Hamilton syringe. The pups were monitored until recovered on a heating pad and returned to the cage for parental care. At P30 mice were perfused for brain collection. Mice were anesthetized with 200 mg/kg tribromoethanol (Avertin) and perfused with TBS/heparin and 4% PFA. The brains were collected and fixed overnight in 4% PFA solution. On the following day, the brains were washed with TBS to remove any residual PFA and cryoprotected in 30% sucrose. The brains were stored at -80°C in a solution containing 2 parts 30% sucrose and 1-part O.C.T. (TissueTek). The day before immunostaining the brains were sectioned using a cryostat to obtain floating coronal tissue sections of 40 µm thickness. The sections were stored in a 1:1 mixture of TBS/glycerol at -20°C. For immunostaining, the sections were washed in 1x TBS containing 0.2% Triton X-100 (TBST) for 10 minutes 3 times at room temperature, and then blocked in 10% NGS diluted in TBST. Following blocking the sections were incubated in primary antibody for 48hs at 4°C with shaking. After incubation with primary antibodies, the sections were washed in TBST for 10 minutes 3 times at room temperature, and incubated in Alexa Fluor conjugated secondary antibodies diluted 1:200 (Life Technologies) for 2 hours at room temperature shaking. After this incubation, the sections were washed 3 times with TBST for 10 minutes and mounted onto glass slides using a homemade mounting media (90% glycerol, 20 mM Tris pH 8.0, 0.5% n-propyl gallate) and sealed with nail polish. For inhibitory synapses we stained with antibodies against HA, VGAT and gephyrin. For somatostatin + synapses we stained with antibodies against HA, somatostatin and gephyrin. For perisomatic PV + synapses we stained with antibodies against HA, Syt2, NeuN and gephyrin. The resulting sections were imaged within 2 days at high magnification (93× objective) with 1.5X zoom factor for inhibitory synapses and somatostatin + synapses and 1.9X zoom factor for Syt2+ synapses, resolution (0.34 µm step size, 1 µm z-stack) on a confocal Leica Stellaris 8 microscope. The images were then processed using a custom pipeline that includes thresholding of each antibody signal and quantification of number of colocalizing puncta. VGAT/gephyrin synapse colocalization and SST/gephyrin synapse colocalization was analyzed using SynBot.⁸¹ Syt2/gephyrin synapses contacting NeuN+ soma was analyzed using a custom-made software available at https://github.com/Eroglu-Lab/Irala_2024_image_analysis.

Proteomic analysis**In vivo TurboID protein purification**

In vivo TurboID experiments were performed as previously described in Takano et al. with modifications.⁵¹ CD1 P1 mouse pups were anesthetized by hypothermia and 1 μl of each concentrated AAV-TurboID vector was injected bilaterally into the cortex using a Hamilton syringe. Pups were monitored until recovered on a heating pad. At P18, P19 and P20 biotin was subcutaneously injected at 24 mg/kg to increase the biotinylation efficiency. 4 mice of both sexes were used for each TurboID condition. At P21 the cerebral cortices were removed and stored at -80° C. For the protein purification, each cortex was lysed in a buffer containing 50 mM Tris/HCl, pH 7.5; 150 mM NaCl; 1 mM EDTA; protease inhibitor mixture (Roche); and phosphatase inhibitor mixture (PhosSTOP, Roche). Next, an equal volume of buffer containing 50 mM Tris/HCl, pH 7.5; 150 mM NaCl; 1 mM EDTA; 0.4 % SDS; 2 % TritonX-100; 2 % deoxycholate; protease inhibitor mixture; and phosphatase inhibitor mixture was added to the samples, following by sonication and centrifugation at 15,000 g for 10 min. The remaining supernatant was ultracentrifuged at 100,000g for 30min at 4° C. Finally, SDS detergent was added to the samples and heated at 45 ° C for 45 min. After cooling on ice, each sample was incubated with High Capacity streptavidin agarose beads (ThermoFisher) at 4° C overnight. Following incubation, the beads were serially washed: 1) twice with a solution containing 2% SDS; 2) twice with a buffer 1% TritonX-100, 1% deoxycholate, 25 mM LiCl; 3) twice with 1M NaCl and finally five times with 50 mM ammonium bicarbonate. The biotinylated proteins attached to the agarose beads were eluted in a buffer 125 mM Tris/HCl, pH6.8; 4 % SDS; 0.2 % β-mercaptoethanol; 20 % glycerol; 3 mM biotin at 60°C for 15min.

Sample preparation

The Duke Proteomics and Metabolomics Core Facility (DPMCF) received 16 samples (4 of each NCAN Nter, NCAN Cter, NCAN IGK, and NCAN cyto) which were kept at -80°C until processing. Samples were spiked with undigested bovine casein at a total of either 1 or 2 pmol as an internal quality control standard. Next, samples were supplemented with 10.6 μL of 20% SDS, a final concentration of 1.2% phosphoric acid and 580 μL of S-Trap (Protifi) binding buffer (90% MeOH/100mM TEAB). Proteins were trapped on the S-Trap micro cartridge, digested using 20 ng/μL sequencing grade trypsin (Promega) for 1 hr at 47C, and eluted using 50 mM TEAB, followed by 0.2% FA, and lastly using 50% ACN/0.2% FA. All samples were then lyophilized to dryness. Samples were resolubilized using 120 μL of 1% TFA/2% ACN with 12.5 fmol/μL yeast ADH.

LC-MS/MS analysis

Quantitative LC/MS/MS was performed on 3 μL (25% of total sample) using an MClass UPLC system (Waters Corp) coupled to a Thermo Orbitrap Fusion Lumos high resolution accurate mass tandem mass spectrometer (Thermo) equipped with a FAIMSPro device via a nanoelectrospray ionization source. Briefly, the sample was first trapped on a Symmetry C18 20 mm × 180 μm trapping column (5 μL/min at 99.9/0.1 v/v water/acetonitrile), after which the analytical separation was performed using a 1.8 μm Acuity HSS T3 C18 75 μm × 250 mm column (Waters Corp.) with a 90-min linear gradient of 5% to 30% acetonitrile with 0.1% formic acid at a flow rate of 400 nanoliters/minute (nL/min) with a column temperature of 55C. Data collection on the Fusion Lumos mass spectrometer was performed for three difference compensation voltages (-40V, -60V, -80V). Within each CV, a data-dependent acquisition (DDA) mode of acquisition with a r=120,000 (@ m/z 200) full MS scan from m/z 375–1500 with a target AGC value of 4e5 ions was performed. MS/MS scans were acquired in the ion trap in Rapid mode with a target AGC value of 1e4 and max fill time of 35 ms. The total cycle time for each CV was 0.66s, with total cycle times of 2 sec between like full MS scans. A 20s dynamic exclusion was employed to increase depth of coverage. The total analysis cycle time for each injection was approximately 2 hours.

Quantitative data analysis

Following UPLC-MS/MS analyses, data were imported into Proteome Discoverer 2.5 (Thermo Scientific Inc.). In addition to quantitative signal extraction, the MS/MS data were searched against the SwissProt *M. musculus* database (downloaded in Nov 2019) and a common contaminant/spiked protein database (bovine albumin, bovine casein, yeast ADH, etc.), and an equal number of reversed-sequence “decoys” for false discovery rate determination. Sequest with Infernys enabled (v 2.5, Thermo PD) was utilized to produce fragment ion spectra and to perform the database searches. Database search parameters included variable modification on Met (oxidation). Search tolerances were 2ppm precursor and 0.8Da production with full trypsin enzyme rules. Peptide Validator and Protein FDR Validator nodes in Proteome Discoverer were used to annotate the data at a maximum 1% protein false discovery rate based on q-value calculations. Peptide homology was addressed using razor rules in which a peptide matched to multiple different proteins was exclusively assigned to the protein that has more identified peptides. Protein homology was addressed by grouping proteins that had the same set of peptides to account for their identification. A master protein within a group was assigned based on % coverage.

Prior to imputation, a filter was applied such that a peptide was removed if it was not measured in at least 2 unique samples (50% of a single group). After that filter, any missing data missing values were imputed using the following rules: 1) if only one single signal was missing within the group of three, an average of the other two values was used or 2) if two out of three signals were missing within the group of three, a randomized intensity within the bottom 2% of the detectable signals was used. To summarize the protein level, all peptides belonging to the same protein were summed into a single intensity. These protein levels were then subjected to a normalization in which the top and bottom 10 percent of the signals were excluded and the average of the remaining values was used to normalize across all samples. These normalized protein level intensities were used for the remainder of the analysis.

Electrophysiology

For whole-cell patch-clamp recordings, 3–4 mice were used for miniature inhibitory postsynaptic current (mIPSC) and miniature excitatory postsynaptic current (mEPSC) for each genotype. During all recordings, brain slices were continuously perfused with standard aCSF at RT (~25°C) and visualized by an upright microscope (BX61WI, Olympus) through a 40x water-immersion objective equipped with infrared-differential interference contrast optics in combination with digital camera (ODA-IR2000WCTRL). Patch-clamp recordings were performed using an EPC 10 patch-clamp amplifier, controlled by Patchmaster Software (HEKA). Data were acquired at a sampling rate of 50 kHz and low-pass filtered at 6 kHz.

To prepare acute brain slices, after decapitation, the brains were immersed in ice-cold artificial cerebrospinal fluid (aCSF, in mM): 125 NaCl, 2.5 KCl, 3 mM MgCl₂, 0.1 mM CaCl₂, 10 glucose, 25 NaHCO₃, 1.25 NaHPO₄, 0.4 L-ascorbic acid, and 2 Na-pyruvate, pH 7.3–7.4 (310 mosmol). Coronal slices containing the ACC were obtained using a vibrating tissue slicer (Leica VT1200; Leica Biosystems). Slices were immediately transferred to standard aCSF (37°C, continuously bubbled with 95% O₂ – 5% CO₂) containing the same as the low-calcium aCSF but with 1 mM MgCl₂ and 1–2 mM CaCl₂. After 30 min incubation, slices were transferred to a recording chamber with the same extracellular buffer at room temperature (RT: ~25°C).

To measure mIPSCs, the internal solution contained the following (in mM): 77 K-gluconate, 77 KCl, 10 HEPES, 1 EGTA, 4.5 MgATP, 0.3 NaGTP, and 10 Na-phosphocreatine, pH adjusted to 7.2–7.4 with KOH and osmolality set to ~ 300 mOsm. mIPSCs were measured in the aCSF bath solution containing 1 μM tetrodotoxin and 10 μM 6-cyano-7-nitroquinoxaline-2,3-dione (CNQX) and 50 μM D-2-amino-5-phosphonopentanoate (D-AP5) at -70 mV in voltage-clamp mode. Series resistance was monitored throughout all recordings and only recordings that remained stable over the recording period (≤ 30 MΩ resistance and <20% change in resistance) were included. mIPSCs recorded at -70 mV were detected and analyzed using Minhee Analysis software (https://github.com/parkgilbong/Minhee_Analysis_Pack)¹. To analyze the frequency, events were counted over 5 minutes of recording. To obtain the average events for each cell, at least 100 non-overlapping events were detected and averaged. The peak amplitude of the average mIPSC was measured relative to the baseline current and only events larger than 5 pA were included. Rise time was defined as the time from 10%–90% of the peak. Rise time analysis was performed using Stimfit software (<https://github.com/neurodroid/stimfit>) and events larger than 10 pA were included. To measure mEPSCs, the internal solution contained the following (in mM): 125 K-gluconate, 10 NaCl, 10 HEPES, 0.2 EGTA, 4.5 MgATP, 0.3 NaGTP, and 10 Na-phosphocreatine, pH adjusted to 7.2–7.4 with KOH and osmolality set to ~ 300 mOsm. mEPSCs were measured in the aCSF bath solution containing 1 μM tetrodotoxin and 50 μM Picrotoxin at -70 mV in voltage-clamp mode. mEPSCs recorded at -70 mV were detected using Stimfit software (<https://github.com/neurodroid/stimfit>). To analyze the frequency, events were counted over 5 minutes of recording. To obtain the average events for each cell, at least 100 non-overlapping events were detected and averaged. The peak amplitude of the average mEPSC was measured relative to the baseline current. All chemicals were purchased from Sigma-Aldrich or Tocris. All chemicals were purchased from Sigma-Aldrich or Tocris.

Transmission electron microscopy

For EM analysis of mouse ACC, P30 NCAN WT controls and KO littermates (3 mice per genotype/age) were first anesthetized with 200 mg/kg tribromoethanol (Avertin) and transcardially perfused with PBS solution to clear out blood cells, and then with 2% PFA, 2.5% glutaraldehyde, 2 mM CaCl₂, and 4 mM MgCl₂ in 0.1 M cacodylate buffer (pH 7.4). 400 μm thick coronal sections per mouse were cut with a blade and the ACC area was dissected out with a scalpel blade. The slices were immersed in 2% glutaraldehyde, 2 mM CaCl₂, and 4 mM MgCl₂ in 0.1 M cacodylate buffer (pH 7.4) and fixed overnight at 4°C. At the Duke Electron Microscopy Service core facility, slices were rinsed in 0.1 M phosphate buffer and postfixed in 1% OsO₄. Next, the samples were dehydrated in ethanol/acetone and incubated in 50:50 acetone:epoxy overnight at room temperature. Ultrathin serial sections were cut and imaged at the Duke Electron Microscopy Service core facility. Inhibitory synapses (symmetric synapses) were identified and counted when presenting a thin postsynaptic density and oval shape presynaptic vesicles. Ten images per brain from 3 sex-matched littermate groups were analyzed.

QUANTIFICATION AND STATISTICAL ANALYSIS

To quantify cell and synapse density sex-matched littermates were used. Brains from each condition were strictly processed, imaged and analyzed together to minimize variability. Multiple litters were used for each experiment. Analyses were repeated and performed blindly. The normalization of synaptic density *in vivo* was performed as previously shown in Risher et al.⁶². Briefly, the synapse density of each KO or mutant mice was divided by the average of the WT mice. This normalization does not affect the stringency of statistics but removes the variability between experiments.

SynBot software

In vitro and *in vivo* excitatory, inhibitory and somatostatin positive synapses were analyzed using open-source ImageJ-based software, SynBot.⁸¹ *In vitro*: confocal single focal plane images were converted to RGB. A fixed threshold was automatically used for all images. Puncta size of 6–8 pixels were used for each experiment. Synapses in a circular area of 3000 μm² around the cell body of each neuron was quantified. *In vivo*: each z-stack image contains 15 optical sections spaced 0.34 μm apart. Maximum projection images representing 1 μm in the z-direction were generated for analysis. Images were deconvolved using TruSight deconvolution

system from Olympus Olympus FV3000 confocal. Each image was manually thresholded. Puncta size of 8–10 pixels were used for each experiment. Synapses were quantified using all the image area. For each genotype, 6 sex-matched P30 littermates mice were analyzed, 3 sections for each animal, L1, L2-3 and L5 of the ACC.

Macro for synapse analysis around cell soma

This in house made macro is available at https://github.com/Eroglu-Lab/Irala_2024_image_analysis. This macro was adapted from SynBot software to quantify colocalization of pre and postsynaptic markers, but using a cell body mask as the area of interest. For parvalbumin (Syt2+) synapse counting we identified pyramidal neuron somas with NeuN antibody. Each z-stack image contains 15 optical sections spaced 0.34 μm apart. Maximum projection images representing 1 μm in the z-direction were generated for analysis. Each image was manually thresholded. NeuN signal was expanded 10 pixels in each direction to capture synapses around the cell body of excitatory neurons. Puncta size of 8–10 pixels were used for each experiment. This macro also calculates the circumference distance of each soma. For each genotype, 6 sex-matched P30 littermates mice were analyzed, 3 sections for each animal, L2-3 and L5 of the ACC.

Macro for area of colocalization smRNA FISH

This in house made macro is available at https://github.com/Eroglu-Lab/Irala_2024_image_analysis. This macro was adapted from SynBot software to quantify the area of colocalization of two colors. Each z-stack image contains 6 optical sections spaced 0.34 μm apart. Maximum projection images representing 1 μm in the z-direction were generated for analysis. Each image was manually thresholded. Area of the mRNA colocalizing with area of GFP positive astrocyte was analyzed using the whole image area. For each timepoint (P7, P15, P21 and P30) 3 animals were analyzed, 3 sections for each animal, L1, L2-3 and L5 of the ACC.

GraphPad Prism 9 was used for all statistical analyses including Student's t-test and one-way ANOVA followed by post-hoc Tukey's test or Dunnett's test when appropriate. Data was plotted as a super plot to visualize individual data points and averages for each experiment when possible. Each figure legend indicates the n for each experiment and the statistical test used. All data are represented as mean \pm standard error of the mean. On each graph, the exact P-value is indicated in the figure. Sample sizes were determined based on previous experience for each experiment to yield high power to detect specific effects. No statistical methods were used to predetermine the sample size. All animals were healthy at the time of analysis and both males and females were equally included in the analysis of each experiment.